PAPER • OPEN ACCESS

Optimised ‘hybrid’ scenario H-mode plasmas for W radiation control in JET with the Be/W wall

OPEN ACCESS
IOP Publishing | International Atomic Energy Agency
Nuclear Fusion
Nucl. Fusion **66** (2026) 036018 (23pp)
https://doi.org/10.1088/1741-4326/ae3b53

Optimised 'hybrid' scenario H-mode plasmas for W radiation control in JET with the Be/W wall

A.R. Field[1,*], C. Angioni[2], I.S. Carvalho[3], P. Carvalho[3], C.D. Challis[1], A. Chomiczewska[4], I.H. Coffey[1,5], D. Fajardo[2], L. Frasinetti[6], J.M. Fontdecaba[7], C. Giroud[1], J. Hobirk[2], A. Kappatou[2], D. Keeling[1], D.B. King[1], D. Kos[1], B. Labit[8], E. Lerche[1,9], E. Litherland-Smith[1], S. Menmuir[1], C. Olde[1], H. Sun[1], N. Vianello[10,11], S. Wiesen[12], JET Contributors[a] and the EUROfusion Tokamak Exploitation Team[b]

[1] United Kingdom Atomic Energy Authority, Culham Campus, Abingdon OX14 3DB, United Kingdom of Great Britain and Northern Ireland
[2] Max-Planck-Institut für Plasmaphysik, Boltzmannstrasse 2, Garching D-58748, Germany
[3] Instituto de Plasmas e Fusão Nuclear (IPFN), Instituto Superior Técnico (IST), Universidade de Lisboa, Av. Rovisco Pais 1, 1049-001 Lisboa, Portugal
[4] Institute of Plasma Physics and Laser Microfusion (IPPLM), 23 Hery Street, Warsaw 01-497, Poland
[5] Astrophysics Research Centre, School of Mathematics and Physics, Queen's University Belfast, Belfast BT7 1NN, United Kingdom of Great Britain and Northern Ireland
[6] Division of Fusion Plasma Physics, KTH Royal Institute of Technology, Stockholm, Sweden
[7] Laboratorio Nacional de Fusión, CIEMAT, Madrid, Spain
[8] Swiss Plasma Center (SPC), Ecole Polytechnique Fédérale de Lausanne (EPFL), Lausanne, Switzerland
[9] LPP-ERM-KMS, EUROfusion Consortium Member, Trilateral Euregio Cluster, TEC partner, Brussels, Belgium
[10] Consorzio RFX (CNR, ENEA, INFN, Universitá di Padova, Acciaierie Venete SpA), Corso Stati Uniti 4, Padova 35127, Italy
[11] Istituto per la Scienza e la Tecnologia dei Plasmi, CNR, Padova, Italy
[12] Forschungszentrum Jülich GmbH, Institut für Energie- und Klimaforschung-Plasmaphysik, Jülich 52425, Germany

E-mail: anthony.field@ukaea.uk

Received 16 June 2025, revised 5 January 2026
Accepted for publication 21 January 2026
Published 4 February 2026

Abstract

Screening of high-Z (W) impurities from the confined plasma by the temperature gradient at the plasma periphery of fusion-grade H-mode plasmas was demonstrated for the first time in JET with the Be/W wall (Field *et al* 2023 *Nucl. Fusion* **63** 016028). Additional experiments have been performed in JET during 2023, including in deuterium–tritium (DT) during the DTE3 campaign, to further optimise the impurity screening in such plasmas, as well as our bolometric measurements of the W impurity fluxes between and during edge-localised modes. A decrease

[a] See Maggi *et al* 2024 (https://doi.org/10.1088/1741-4326/ad3e16) for JET Contributors.
[b] See Joffrin *et al* 2024 (https://doi.org/10.1088/1741-4326/ad2be4) for the EUROfusion Tokamak Exploitation Team.
[*] Author to whom any correspondence should be addressed.

in plasma current from 2.3 MA to 2.1 MA reduced the electron density and thereby increased the ion temperature at the H-mode pedestal top, resulting in stronger impurity screening behaviour. The scenario was then successfully transferred to operation in DT by increasing the toroidal field, in order to compensate the lower L/H-threshold power in DT compared to D plasmas. Here, results of detailed analysis and modelling of the neoclassical (NC) W transport in four pulses from these experiments are presented, two in D at 2.3 MA and 2.1 MA plasma current and a matched pulse pair at 2.1 MA in D and DT. Using the FACIT code (Fajardo *et al* 2023 *Plasma Phys. Control. Fusion* **65** 035021) to model the NC W transport for these more recent pulses, the outward convection just inside the pedestal top found in our earlier study could not be reproduced. Possible reasons for this discrepancy between experimental observations and our modelling results are discussed, including potential deficiencies in our measurement technique and/or incompleteness of the NC transport modelling.

Keywords: impurities, tungsten, screening, hybrid, H-mode, pedestal

(Some figures may appear in colour only in the online journal)

1. Introduction

Control of the W content of the confined plasma can be achieved by impurity screening at the edge of a tokamak plasma, provided the ion temperature gradient T_i' is strong enough with respect to the electron density gradient n_e', leading to outward neoclassical (NC) convection of tungsten [1, 2]. Such 'temperature-gradient screening' has been predicted for ITER conditions [3, 4].

Such peripheral impurity screening was observed experimentally for the first time in 'hybrid' scenario, type-I ELMy, deuterium (D) plasmas [5] in JET with an all-metal (Be/W) first-wall (JET-Be/W) [6], as originally intended for ITER [7]. Similar observations were reported from the second JET deuterium–tritium (DT) campaign (DTE2) [8]. The screening strength was found to be enhanced by the strong toroidal rotation and low collisionality at the periphery of these plasmas [9], as was also the case in small-edge-localised mode (ELM) regime H-mode plasmas in JET [10], achieved at high heating power and low gas fuelling rates.

During 2023, further experiments were carried out on JET-Be/W, both in DT during the DTE3 campaign [11] and in D during the campaigns before and after DTE3, with the aim of further studying the peripheral W screening in hybrid-scenario pulses at high heating power ($P_{in} \gtrsim 30$ MW). Details of the associated scenario development, to optimise both the peripheral W screening and the performance of the necessary diagnostics are described in [12]. Here, we focus instead on the detailed analysis of a selection of these recent pulses in terms of their evolution, performance and inter-ELM impurity dynamics. Results of interpretive modelling of the neoclassical (NC) W transport are also presented, with the aim of determining the location at which the W screening occurs.

The remainder of this paper is structured as follows: The methodology for further optimisation of the hybrid-scenario pulses in D for W screening and how it was adapted for DT pulses run during the DTE3 campaign is explained in section 2. The effect of decreasing the plasma current on plasma performance is investigated in section 3: in terms of their overall performance and pedestal parameters in section 3.1; the evolution of the total radiation distribution as a proxy for the behaviour of the W impurities is described in sections 3.2 and 3.3; quantification of the W flushing by ELMs and the inter-ELM W influx (or screening) from analysis of bolometric total radiation data is described in section 3.4; modelling of the NC W transport and comparison with bolometric total radiation measurements is presented in sections 3.5 and 3.6 respectively; a discussion then follows in section 3.7. The same structure then follows in section 4, which compares a matched pair of optimised hybrid-scenario pulses in D and DT. Finally, a general discussion of the results is presented in section 5 and our overall conclusions in section 6.

2. Further optimisation of 'hybrid' scenario pulses:

In the JET-Be/W campaigns run just before and after the third DT campaign (DTE3) in 2023, experiments were performed with the goal of further optimising the temperature-gradient screening of W impurities that was first reported in a study of pulses from earlier experiments [5]. The the various steps taken to optimise the scenario are discussed in detail in [12].

The key to achieving conditions for peripheral W screening in hybrid-scenario plasmas has been the optimisation of the gas fuelling at the beginning of the heating phase [8], both in terms of the fuelling rate and timing to achieve low pedestal density $n_{e,ped}$, high pedestal ion temperature $T_{i,ped}$ at high heating power P_{in} and hence low pedestal collisionality and a high toroidal angular velocity at the pedestal top $\Omega_{\phi\,i,ped}$.

In the most recent experiments [12], in D plasmas, variation of the pedestal density was achieved by varying the initial fuelling rate and timing and by reducing the plasma current from the 2.3 MA/3.45 T pulses studied in [5] down to 2.1 MA. Attempts were also made to vary the toroidal rotation by changing the NBI tangency radius, although this had limited effect.

During the DTE2 campaign, studies of the W screening in DT plasmas were hampered by the fact that the horizontal bolometry camera was affected by the T_2 gas fuelling from

a nearby main chamber Tritium-Injection Module (TIM) [8]. Hence, special efforts were taken to avoid this in the DTE3 experiments, with only a TIM in the divertor region used for the T_2 gas fuelling during the sustained phase to avoid compromising the horizontal bolometry camera measurements. Pulses that completely avoided the use of any of the main-chamber TIMs were also obtained to minimise any such effect on the data.

To compensate for the use of D-only NBI during the DTE3 campaign, the pulses were designed to be T-rich in the current ramp-up. By tuning the H-mode entry as described in [8], a very good match with the earlier D pulse #97781, in which the impurity screening behaviour was first clearly demonstrated [5], was achieved in terms of radiated power and edge parameters.

Further improvement was achieved by increasing the magnetic field from 3.45 T to 3.85 T, thereby increasing the L–H power threshold P_{LH}, allowing the same heating power ramp to be used as in D plasmas without entering H-mode too early. As a result of this optimisation, the very high $T_{\mathrm{i,ped}} \lesssim 3.5\,\mathrm{keV}$ was achieved, albeit transiently, in the DT pulse #104681 at $2.1\,\mathrm{MA}/3.85\,\mathrm{T}$ with heating power $P_{\mathrm{in}} \sim 35\,\mathrm{MW}$ with no main chamber T_2 gas fuelling used at all. The matched pulse in D #105508 was subsequently performed with the same engineering parameters as the DT pulse #104681 for the purpose of comparison.

3. Influence of plasma current on impurity control

In this section, the effect of reducing the plasma current from 2.3 MA to 2.1 MA on the pulse evolution, pedestal parameters, the total radiation and the W impurity transport (flushing/screening) across the pedestal gradient region are analysed in detail through comparison of the evolution of the matched pair of hybrid-scenario D pulses #102813 (at 2.3 MA) and #102825 (at 2.1 MA), both run at 3.45 T toroidal field with similar total heating power $P_{\mathrm{in}} \sim 35\,\mathrm{MW}$ from NBI ($P_{\mathrm{NBI}} \sim 30\,\mathrm{MW}$) and ICRH ($P_{\mathrm{RF}} \sim 5\,\mathrm{MW}$), as shown in figure 1(*a*).

3.1. Pulse start-up and evolution

Key to achieving the conditions for peripheral impurity screening is optimisation of the initial gas fuelling. The gas fuelling rate waveform shown in figure 1(*b*) has an initial phase with a low fuelling rate to achieve a hot, low collisionality pedestal, followed by a pulse of gas to induce ELMs, thereby preventing a long initial ELM-free period with a high-amplitude first ELM.

As can be seen from figure 1(*c*), the radiated power remains fairly constant over the flat-top phase of the pulses, i.e. not running away due to uncontrolled impurity influx and/or accumulation. The radiated power fraction from the confined plasma $\mathcal{F}^{\mathrm{Pl}}_{\mathrm{Rad}} = P^{\mathrm{Pl}}_{\mathrm{Rad}}/P_{\mathrm{in}}$ is lower ($\sim$40%) in the lower current pulse #102825 than in the higher current pulse #102813 ($\sim$60%), which also exhibits a $\sim$0.6 s period of higher radiation ($\mathcal{F}^{\mathrm{Pl}}_{\mathrm{Rad}} \sim 70\%$) due to an impurity event at $\sim$8.6 s.

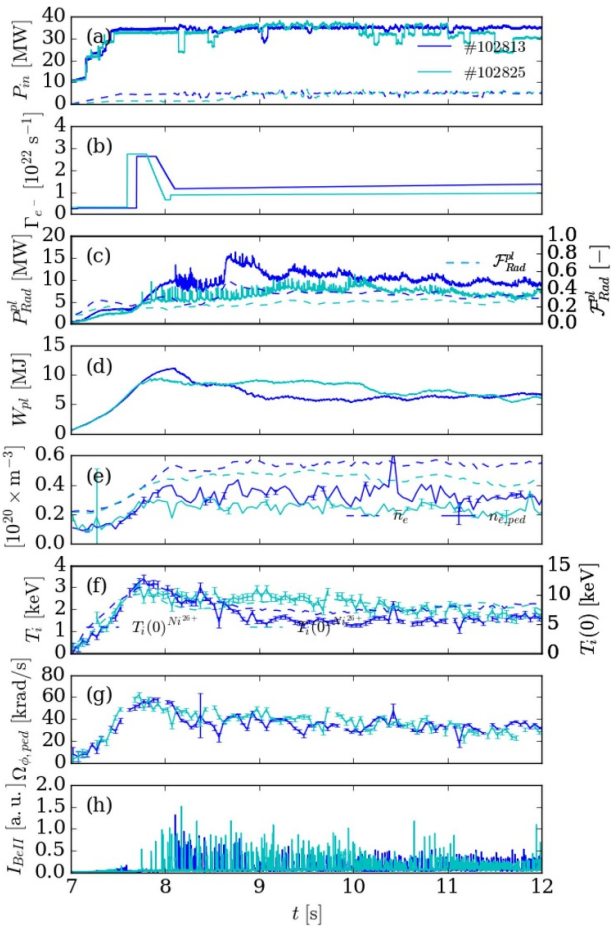

Figure 1. Comparison of the evolution of two hybrid-scenario D pulses #102813 (blue) (at 2.3 MA/3.45 T) and #102825 (cyan) (at 2.1 MA/3.45 T) showing: (*a*) the total heating power P_{in} from NBI and ICRH heating; (*b*) the requested D_2 gas-fuelling rate waveform (in e/s) Γ_{e^-}; (*c*) the radiated power from the confined plasma $P^{\mathrm{Pl}}_{\mathrm{Rad}}$; (*d*) the plasma stored energy W_{pl} from magnetic equilibrium reconstructions using EFIT++; (*e*) the pedestal electron density $n_{\mathrm{e,ped}}$ (solid) and line-averaged density $\bar{n}_{\mathrm{e}}$ (dashed); (*f*) the ion temperature at the density pedestal top $T_{\mathrm{i,ped}}$ measured by CXRS [15] (solid) and the central ion temperature $T_{\mathrm{i},0}$ measured by high-resolution spectroscopy of Ni^{+26} ions [16] (dashed); (*g*) the toroidal angular velocity at the density pedestal top $\Omega_{\phi\,\mathrm{i,ped}}$; and (*h*) the ELM behaviour from a visible Be II line intensity measured viewing the outer divertor target.

The plasma stored energy W_{pl}, obtained from magnetic equilibrium reconstructions using the EFIT++ code [13, 14], run using magnetics data only, is shown in figure 1(*d*). In the 2.3 MA pulse #102813, $W_{\mathrm{pl}} \lesssim 12\,\mathrm{MJ}$ decreases twice, first at the end of the overshoot phase to $\sim$10 MJ and again to $\sim$7 MJ after the increase in P_{Rad} due to the impurity event. Analysis of magnetic measurements shows that an $n = 3$ MHD mode starts after the overshoot phase at $\sim$8.6 s, which is one cause of the reduction in energy confinement.

In the lower current 2.1 MA pulse #102825, the initial value of $W_{\mathrm{pl}} \sim 9\,\mathrm{MJ}$ is lower than in the lower current pulse but is sustained for longer, consistent with the higher safety factor q, until a reduction to $\sim$7 MJ after $\sim$10.2 s, when an $n = 3$ MHD

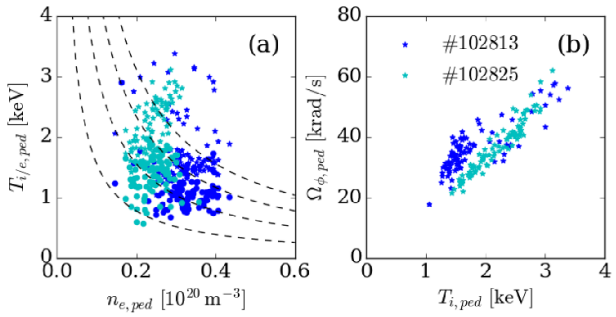

Figure 2. Comparison of pedestal parameters for the hybrid-scenario pulses #102813 (at 2.3 MA) and #102825 (at 2.1 MA) showing: (*a*) $T_{\mathrm{e,ped}}$ (•) and $T_{\mathrm{i,ped}}$ ($\star$) vs' $n_{\mathrm{e,ped}}$; and (*b*) $\Omega_{\phi\mathrm{i,ped}}$ vs' $T_{\mathrm{i,ped}}$, where $T_{\mathrm{i,ped}}$ and $\Omega_{\phi\mathrm{i,ped}}$ are determined at the density pedestal top and the data are from the time period 7.5–12 s.

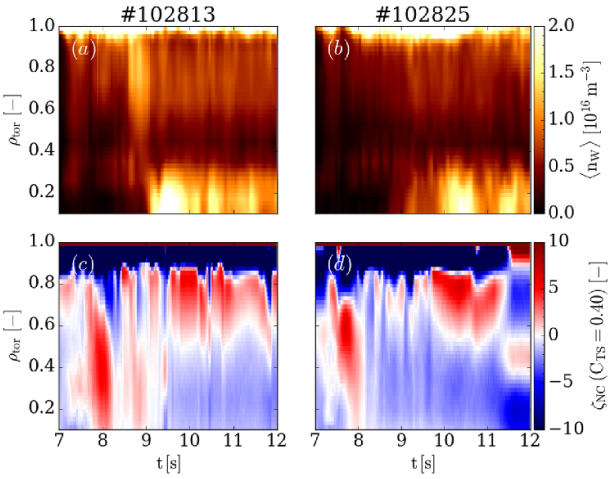

Figure 3. Comparison of the two hybrid-scenario D pulses #102813 at 2.3 MA (left) and #102825 2.1 MA (right), showing the profile evolution of: (*a*), (*b*) a proxy for the FSA W density distribution $\langle n_{\mathrm{W}} \rangle^{\star} = \langle \epsilon_{\mathrm{tot}} \rangle / (n_{\mathrm{e}} \mathcal{R}_{\epsilon})$, where the total emission coefficient $\mathcal{R}_{\epsilon}$ is assumed constant; and (*c*), (*d*) a proxy for the NC convection ζ_{NC}, calculated assuming a constant value of the screening parameter $C_{\mathrm{TS}} = 0.4$, vs' ρ_{tor}.

mode appears, albeit at a weaker amplitude than in the other pulse.

The hybrid-scenario, with elevated central safety factor $q_0 \gtrsim 1.5$ and a broad flat central q-profile is formed by strong NBI heating during the initial current ramp of a low density target plasma [8]. This results in the formation of a transient internal transport barrier (ITB), with reduced core heat transport and high central ion temperature $T_{\mathrm{i},0} \lesssim 12\,\mathrm{keV}$ (see figure 1(*f*)).

As the pedestal density tends to increase with the plasma current [17], in the lower current pulse #102825 it is a factor ∼30% lower ($n_{\mathrm{e,ped}} \sim 2.5 \times 10^{19}\,\mathrm{m}^{-3}$) than in the higher current pulse #102813 ($\sim 3.5 \times 10^{19}\,\mathrm{m}^{-3}$) (see figure 1(*e*)). The line-averaged density $\bar{n}_{\mathrm{e}}$ is reduced by a smaller factor (∼15%) than that of the pedestal density ($\bar{n}_{\mathrm{e}} \lesssim 6 \times 10^{19}\,\mathrm{m}^{-3}$ in pulse #102813 and $\lesssim 5 \times 10^{19}\,\mathrm{m}^{-3}$ in pulse #102825). Hence, in the lower current pulse, the density profile is more peaked than in the higher current pulse.

The lower $n_{\mathrm{e,ped}}$ at the lower current results in a higher $T_{\mathrm{i,ped}} \sim 1.5\,\mathrm{keV}$ in the lower current pulse cf ∼1.2 keV at the higher current during the flat-top phase (see figure 1(*f*)), while during the initial 'over-swing' phase prior to the ELMs, $T_{\mathrm{i,ped}} \lesssim 3\,\mathrm{keV}$ is considerably higher. A comparison of the pedestal parameters for the two pulses is shown in figure 2, from which the higher $T_{\mathrm{e,ped}}$ and $T_{\mathrm{i,ped}}$ and lower $n_{\mathrm{e,ped}}$ in the lower current pulse is clearly evident.

The low level of gas fuelling at the start of the pulse also results in an initially high toroidal angular velocity at the pedestal top $\Omega_{\phi\mathrm{i,ped}} \lesssim 50\,\mathrm{krad\,s}^{-1}$ (see figure 1(*g*)). As shown in figure 2, although $\Omega_{\phi\mathrm{i,ped}}$ increases proportionally with $T_{\mathrm{i,ped}}$ in both pulses, the magnitude of $\Omega_{\phi\mathrm{i,ped}}$ is similar, i.e. decreasing I_{p} increases $T_{\mathrm{i,ped}}$ (by decreasing $n_{\mathrm{e,ped}}$) but does not change the edge rotation, which is more affected by the NBI driven torque and charge-exchange viscous drag with the edge neutral gas.

3.2. Evolution of total emissivity profile

Simplified proxies for the flux-surface-averaged (FSA) W density $\langle n_{\mathrm{W}} \rangle$ derived from the FSA total radiated emissivity $\langle \epsilon_{\mathrm{tot}} \rangle$ and for the NC W convection, which is proportional to the parameter $\zeta_{\mathrm{NC}} = C_{\mathrm{TS}} R/L_{T_{\mathrm{i}}} - R/L_{n_{\mathrm{i}}}$, are used here to investigate the behaviour of the W impurities over the core plasma, where a constant value of temperature gradient screening parameter $C_{\mathrm{TS}} = 0.4$ can be assumed. In the outer regions of the plasma, where C_{TS} exhibits significantly smaller values, more detailed calculations of the NC W transport are required, as presented in section 3.5.

The evolution of the FSA total radiated emissivity $\langle \epsilon_{\mathrm{tot}} \rangle$ for the two pulses #102813 and #102825 is shown in figure 7(*d*), from which it can be seen that after the initial overshoot phase, the impurity radiation (which is dominated by that from W) migrates into the plasma core, at about the same time (∼9 s) in both pulses.

For the W impurities, which typically have a mean charge in the core plasma of $\bar{Z} \lesssim 50$, impurity peaking due to NC accumulation can be extreme [18]. For this reason, 5 MW of minority ICRH heating is used in these pulses to inhibit full impurity accumulation by modifying both the background plasma profiles and increasing the turbulent particle transport in the core [19, 20].

Because W dominates the total emissivity, its FSA density can be calculated *approximately* from $\langle n_{\mathrm{W}} \rangle \sim \langle \epsilon_{\mathrm{tot}} \rangle / (\mathcal{R}_{\epsilon} n_{\mathrm{e}})$, using for simplicity the constant value of the total W emissivity coefficient $\mathcal{R}_{\epsilon} \sim 4.5 \times 10^{-31}\,\mathrm{Wm}^3$. The resulting evolution of this proxy for the W density $\langle n_{\mathrm{W}} \rangle^{\star}$ is shown in figures 3(*a*) and (*b*) for the two pulses #102813 and #102825.

A profile of $\mathcal{R}_{\epsilon}$ for pulse #102813 at 10 s is shown in figure 5(*b*), from which it can be seen that $\mathcal{R}_{\epsilon}$ is about a factor of two lower in magnitude in the plasma core than over

the mantle region[13]. Hence, the values of $\langle n_W \rangle^\star$ shown in figures 3(*a*) and (*b*) are underestimates of the actual W density by a similar factor in the core region.

Also shown in figures 3(*c*) and (*d*) is the evolution the parameter $\zeta_{NC} = C_{TS} R/L_{T_i} - R/L_{n_i}$, which is a simplified proxy proportional to the NC convection velocity $V_{NC,Z}$ (see equation (1) of [5]). Here, we have used a constant value of the temperature-gradient screening coefficient $C_{TS} = 0.4$ for calculation of ζ_{NC}, rather than the more usual value of $1/2$ appropriate for the Pfirsch–Schlüter (PS) regime. This value better approximates the values obtained over the core region from detailed modelling using the FACIT code [9], as discussed in section 3.5.2 below.

From this figure, it can be seen that, during the initial overshot phase, the T_i gradient across the core plasma is strong enough for the NC convection to be outward ($\zeta_{NC} > 0$), thereby largely localising the W impurities to the mantle region and preventing their accumulation in the core. Later on, in both pulses, the NC convection reverses ($\zeta_{NC} < 0$) due to a reduction of the T_i gradient across the core, allowing the W impurities to partially accumulate, although an appreciable fraction of the W remains in the mantle.

Note that during these pulses, there is a gradual peaking of the density profile, which, combined with profile changes caused by MHD islands [21], also contributes to the reversal of the NC convection. Note that in both pulses, MHD mode analysis shows that an $n = 3$ mode appears just before the impurities begin to accumulate in the core plasma.

Also, over the mantle region where $\zeta_{NC} > 0$, detailed calculations with the FACIT code [9] (see section 3.5) yield decreasing values of $C_{TS} \sim 0.3$ towards the pedestal top, which reduces the NC convection to $V_{NC,Z} \sim 0$, removing the apparent screening behaviour in this region seen in figures 3(*c*) and (*d*).

Across the pedestal gradient region ($\rho_{tor} > 0.95$) the convection parameter is predominantly strongly negative $\zeta_{NC} \sim \mathcal{O}(-100)$, consistent with a strong inward impurity pinch, which is also confirmed by the more rigorous N–C modelling using the FACIT code.

Interestingly, the FSA W density proxy $\langle n_W \rangle^\star$ is hollow over the pedestal gradient region, i.e. peaks at the separatrix, which is consistent with outward impurity screening rather than an inward pinch. Note that the FSA emissivity profiles $\langle \epsilon_{tot} \rangle$ are also slightly hollow over the pedestal region, although the emissivity profiles $\epsilon_{tot}(R)$ are not hollow at the low-field-side (LFS) mid-plane (see e.g. figures 13 and 14 respectively).

The cause of the hollow FSA emissivity profile can be partly understood from the poloidal distribution of the emissivity $\epsilon_{tot}(\theta)$, which peaks in the lower high-field-side (HFS) scrape-off layer (SOL) region, as seen in figure 4, as is discussed further in section 3.3 below. It is also likely that mid-Z impurities, which are neglected here, e.g. Ni which radiates strongly at $T_e \sim \mathcal{O}(100)$ eV, contribute significantly to the emissivity in the pedestal region.

[13] The mantle region is defined here as $0.7 \leqslant \rho_{tor} \leqslant 0.95$, where the normalised radial coordinate $\rho_{tor} = \Phi_N^{1/2}$ and Φ_N is the normalised toroidal flux.

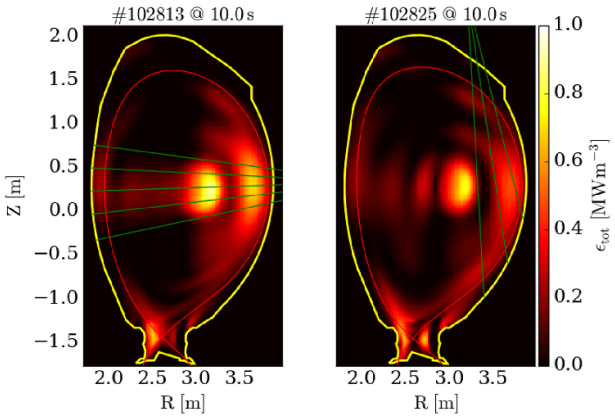

Figure 4. Comparison of the emissivity distribution $\epsilon_{tot}(R,Z)$ from tomographic inversions [22] of bolometric radiation measurements [23] for the two hybrid pulses #102813 (left) and #102825 (right) at 10 s, where outline of the first wall is shown in yellow and the separatrix contour in red. The lines of sight used for the W ELM flushing/screening analysis with data from either the horizontal (KB5H) or the vertical (KB5V) cameras are shown in green in the left/right plots respectively.

For the reasons stated above, the evolution of the quantities shown in figure 3 only approximate those of $\langle n_W \rangle$ and $V_{NC,Z} \propto \zeta_{NC}$, so only their behaviour over the core region should be considered where these proxies are more reliable.

3.3. Total radiation distribution

Distributions of the total radiated emissivity $\epsilon_{tot}(R,Z)$ at 10 s determined from tomographic inversions [22] of bolometric measurements [23] are shown in figure 4 for the two hybrid pulses #102813 and #102825.

Radiation from the confined plasma is distinguished by two main features: in a central region near the magnetic axis and another at the LFS mid-plane. Note that, at this time, the emission from both the core and mantle regions is lower in the lower current pulse #102825 than in the higher current pulse #102813.

There is also strong emission from the HFS divertor region. The finite spatial resolution of the bolometric measurements ($\sim 5 - 10$ cm) causes some spill-over of this emission across the separatrix into the neighbouring region of the pedestal, which is a possible cause of the hollowness of the FSA emissivity profiles $\langle \epsilon_{tot} \rangle$ mentioned in section 3.2 above.

3.4. ELM and inter-ELM W fluences

Relative changes in the W content of the confined plasma $\Delta \bar{n}_W / \bar{n}_W$ due to ELMs and inter-ELM cross-pedestal particle transport are determined from analysis of intensity signals from the multi-channel bolometer system, as described in [5, 24].

Some important differences in the analysis used for the results presented here, which are explained in more detail below,

are: use of data from the vertical-viewing (KB5V) rather than the horizontal-viewing bolometer camera (KB5H) and use of pre- and post-ELM averaging time ranges defined relative to the inter-ELM periods, rather than fixed time intervals, as were used for our earlier work [5].

This approximate analysis [25] relies on several simplifying assumptions, so it is as well to check that these remain valid for the conditions prevailing in the pulses discussed here. Firstly, it is assumed that the total radiated emissivity $\epsilon_{\rm tot}$ is dominated by emission from the W impurities. Secondly, the method relies on the fact that the cooling factor of tungsten $\mathcal{R}_\epsilon$ is relatively constant over temperature range prevailing over the mantle region.

These assumptions, and the fact that the radiated power is proportional to the electron density $n_{\rm e}$, i.e. $P_{\rm Rad} \propto n_{\rm e}\mathcal{R}_\epsilon n_{\rm W}$, where $n_{\rm W}$ is the W density, can be used to determine relative changes in the W content from the relation $\Delta\bar{n}_{\rm W}/\bar{n}_{\rm W} \sim \Delta f_{\rm fl}/f_{\rm fl}$, where the 'flushing' signal $f_{\rm fl} = P^{\rm man}_{\rm Rad}/\bar{n}_{\rm e}$, $P^{\rm man}_{\rm Rad}$ is the total radiation from the mantle region and $\bar{n}_{\rm e}$ the line-averaged density measured along an interferometer chord through the mantle region.

Integrated analysis of $Z_{\rm eff}$[14], soft x-ray (SXR) and total radiation measurements described in [26] was developed to determine relative contributions to $P_{\rm Rad}$ and $Z_{\rm eff}$ and concentrations of the low-Z Be, a representative mid-Z impurity, e.g. Ni and the high-Z W impurities.

As one of the SXR cameras used for this analysis was not available from the DTE2 campaign onwards, it is not possible to perform this analysis for the pulses discussed here. However, analysis of data from the earlier hybrid-scenario pulse #97781 with a similar heating power to those discussed here reveals that W radiation contributes ~70% of the total $P_{\rm Rad}$ and a $\Delta Z_{\rm eff} \sim 0.2$, while for Ni impurities contribute ~25% to $P_{\rm Rad}$ and a $\Delta Z_{\rm eff} \sim 0.7$.

For the hybrid-scenario pulse #102813, figure 5(*b*) shows that the total emissivity coefficient for W is indeed approximately constant over the mantle region at $\mathcal{R}_\epsilon \sim 4.5 \times 10^{-31}\,{\rm W\,m^3}$, where $T_{\rm e}$ is in the range $1-2\,{\rm keV}$ [27]. At the time shown (10 s), the maximum emissivity over the mantle is similar to that in the core. Hence, due to the much larger volume ($\sim \times 4$) of the mantle compared to that of the core ($0 \lesssim \rho_{\rm tor} \lesssim 0.3$), the emission from the mantle dominates the total radiated power.

Using the value of $\mathcal{R}_\epsilon$ stated above, it is possible to estimate that the average W concentration in the mantle region is $\langle C_{\rm W}\rangle_{\rm man} \sim P^{\rm man}_{\rm Rad}/(V_{\rm man}\mathcal{R}_\epsilon \bar{n}_{\rm e}^2)$. Examples of the flushing signal $f_{\rm fl}$ and the derived, average W concentration over the mantle region $\langle C_{\rm W}\rangle_{\rm man}$, which is typically $\sim 1\times10^{-4}$, are shown figure 7(*a*) for the two hybrid-scenario pulses #102813 and #102825.

Provided the above assumptions hold, relative changes in the flushing signal $f_{\rm fl}$ over the intra-ELM and inter-ELM periods, which are $\mathcal{O}(1\,{\rm ms})$ and $\mathcal{O}(10-100\,{\rm ms})$ in duration

[14] The 'effective' ion charge is defined as: $Z_{\rm eff} = \sum n_{\rm i}Z_{\rm i}^2/\sum n_{\rm i}Z_{\rm i}$, where the sum is over all ion species and charge states.

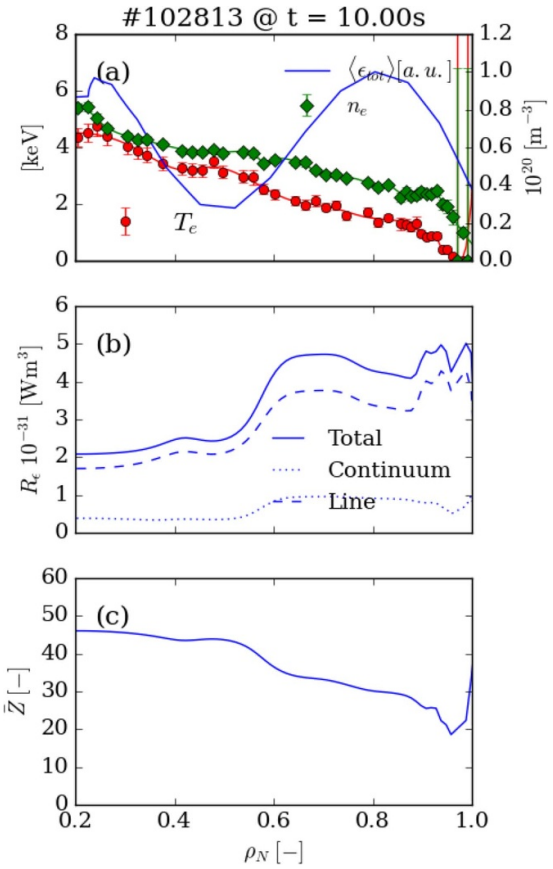

Figure 5. Profiles of (*a*) $T_{\rm e}$ (●), $n_{\rm e}$ (♦) and normalised FAS total emissivity $\langle\epsilon_{\rm tot}\rangle$ from bolometer tomography (blue); (*b*) total emissivity of W $\mathcal{R}_\epsilon$ (solid) with contributions from continuum (dotted) and line radiation (dashed); and (*c*) mean charge state of W in coronal equilibrium $\bar{Z}$ vs' normalised radius $\rho_{\rm tor}$ for the hybrid-scenario pulse #102813 (2.3 MA) at 10 s.

respectively, can be used to quantify relative changes in the W content of the mantle $\Delta\bar{n}_{\rm W}/\bar{n}_{\rm W}$, due to the W fluences (i.e. the time-integrated fluxes) caused by the ELMs and transport across the pedestal between the ELMs respectively. Examples of the signals underlying this analysis are shown in figure 6 and the resulting $\Delta\bar{n}_{\rm W}/\bar{n}_{\rm W}$ data for the two pulses #102813 and #102825 is shown in figure 7(*b*).

Results from such analysis presented in our previous work [5, 24], were produced using intensity data from the central four lines of sight (KB5H channels #12-16) of the horizontal bolometer camera, as shown in figure 4(left). As only relative changes in the signal are used to determine $\Delta\bar{n}_{\rm W}/\bar{n}_{\rm W}$, the sum of the data from these channels is used as a proxy for $P^{\rm man}_{\rm Rad}$.

For two reasons, this method applied to data from the horizontal camera was not considered reliable for the later hybrid-scenario pulses discussed here: Firstly, during DT operations, signals from the horizontal bolometer camera were corrupted by the injection of T_2 gas from the neighbouring main-chamber TIM (TIM-15), which produced a strong contribution to the signal from energetic charge-exchange T^0 atoms from the edge plasma incident on the detector. For this reason, the scenario was modified for DT pulses to use only gas injection

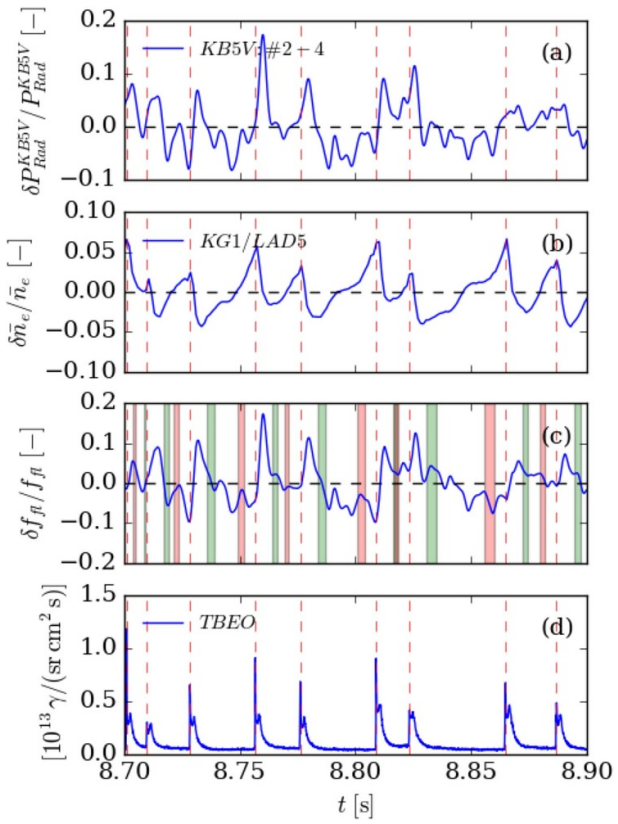

Figure 6. An example of the data used for the W flushing/screening analysis for pulse #102825, showing fractional changes in: (*a*) the radiated power $\delta P_{\mathrm{Rad}}/P_{\mathrm{Rad}}$ from the summed intensity signals of chs. #2–4 of the vertical viewing bolometer camera KB5V; (*b*) the line-averaged density signal $\delta\bar{n}_{\mathrm{e}}/\bar{n}_{\mathrm{e}}$ from ch. #5 of the FIR interferometer; (*c*) the flushing signal $\delta f_{\mathrm{fl}}/f_{\mathrm{fl}}$; and (*d*) the ELM behaviour from the intensity of a BeII line observing the outer divertor target. The red and green bars represent the time ranges for the pre- and post-ELM averaging of $\delta f_{\mathrm{fl}}/f_{\mathrm{fl}}$.

into the main chamber during the initial phase but not during the current 'flat-top' phase.

The second reason not to use data from the horizontal bolometer camera is related to the presence of emission from the core region when some of the impurities have accumulated in the plasma centre, e.g. as is the case for the two pulses shown in figure 4. Even if the W emission and n_{e} in the core region were constant on the time scale of the ELM period, the contribution of this emission to the intensities measured along the horizontal LOS would result in an underestimate of relative changes $P_{\mathrm{Rad}}^{\mathrm{man}}$ and hence in the derived values of $\Delta\bar{n}_{\mathrm{W}}/\bar{n}_{\mathrm{W}}$.

Furthermore, if the radial distribution of the W impurities were to change on the time scale of the ELM period, e.g. move inwards after the ELM crashes due to a steepening of the density gradient across the mantle region, this would result in them moving into a region of higher T_{e} where the W emissivity is lower, resulting in a reduction of the signal for no net change in W content of the plasma. Evaluation of such dynamic effects on the time scale of the ELM cycle is beyond the scope of this work.

Note that if there were to be such prompt inward convection of the W impurities just after the ELMs, this would have to be compensated by outward convection later in the ELM cycle because the total emissivity from the core region remains quite constant, rather than increasing continuously throughout the pulse.

To overcome these difficulties, for these more recent pulses, our analysis has been modified to use instead data from three channels of the vertical bolometer camera (KB5V, channels #2–4), which view through the mantle region but miss the emission from the plasma core (see figure 4(right)). This camera is well removed from any TIMs, hence minimising the issue of contamination of the signal by a contribution from hot CX T^0 atoms. The data shown for the ELM W flushing $(\Delta\bar{n}_{\mathrm{W}}/\bar{n}_{\mathrm{W}})_{\mathrm{ELM}}$ and inter-ELM influx $(\Delta\bar{n}_{\mathrm{W}}/\bar{n}_{\mathrm{W}})_{\mathrm{i-ELM}}$ shown in figure 7(*b*) and subsequent figures is derived using data from the vertical bolometer camera, unless otherwise stated.

In the analysis for our previous publication [5], fixed pre- and post-ELM time ranges for averaging the bolometric data were used, which imposed a rather low limit on the ELM frequency $f_{\mathrm{ELM}} = 1/\Delta t_{\mathrm{ELM}}$ (where Δt_{ELM} is the inter-ELM period) for the validity of the flushing/screening data of $f_{\mathrm{ELM}} \lesssim 50\,\mathrm{Hz}$. For the results presented here, averaging time periods of a fixed fraction of the inter-ELM period of $F_\Delta \times \Delta t_{\mathrm{ELM}}$, where $F_\Delta = 0.1$ are used instead, which results in a higher maximum ELM frequency for the results of the analysis to be valid.

It is still necessary to use fixed time intervals before and after the ELM peak times t_{ELM} to avoid dips in the bolometry signals caused by the low-pass filtering (low-pass cut-off frequency $f_{\mathrm{LP}} = 200\,\mathrm{Hz}$) of the data. The resulting pre-ELM averaging times are then defined as $\{(dt_{\mathrm{pre}} - F_\Delta \Delta t_{\mathrm{ELM}}), dt_{\mathrm{pre}}\}$, where $dt_{\mathrm{pre}} = -4\,\mathrm{ms}$. The post-ELM averaging times for the vertical camera data are defined as $\{dt_{\mathrm{post}}, (dt_{\mathrm{post}} + F_\Delta \Delta t_{\mathrm{ELM}})\}$, where $dt_{\mathrm{post}} = 7.5\,\mathrm{ms}$ for the vertical camera data and 10 ms for the horizontal camera data, which exhibits more 'ringing' due to relatively larger ELM amplitudes.

Using these averaging time intervals, the maximum ELM frequency for the flushing/screening analysis to be valid, i.e. above which these periods would overlap is given by: $f_{\mathrm{ELM}}^{\mathrm{max}} = (1 - 2F_\Delta)/(dt_{\mathrm{pre}} + dt_{\mathrm{post}}) = 70\,\mathrm{Hz}$ for analysis of the vertical camera data and 57 Hz for the horizontal camera data analysis. Any flushing/screening data from inter-ELM periods shorter than $\Delta t_{\mathrm{ELM}}^{\mathrm{min}} = 1/f_{\mathrm{ELM}}^{\mathrm{max}}$ are excluded from the relevant plots and subsequent averaging. As can be seen from figure 7(*c*), this condition for the analysis to be valid is usually met, except during the periods with the highest average ELM frequencies $\langle f_{\mathrm{ELM}} \rangle$, e.g. as occurring later ($\gtrsim 10\,\mathrm{s}$) in pulse #102825.

A comparison of the same $\Delta\bar{n}_{\mathrm{W}}/\bar{n}_{\mathrm{W}}$ data derived using intensity data from either the horizontal or vertical bolometer cameras is shown in figure 8 for the two pulses shown in figure 7(*b*), from which it can be seen that the data derived from the vertical camera exhibits a stronger tendency for an outward inter-ELM W flux, i.e. negative values of $(\Delta\bar{n}_{\mathrm{W}}/\bar{n}_{\mathrm{W}})_{\mathrm{i-ELM}}$, i.e. stronger screening behaviour, than the same data derived from the horizontal camera.

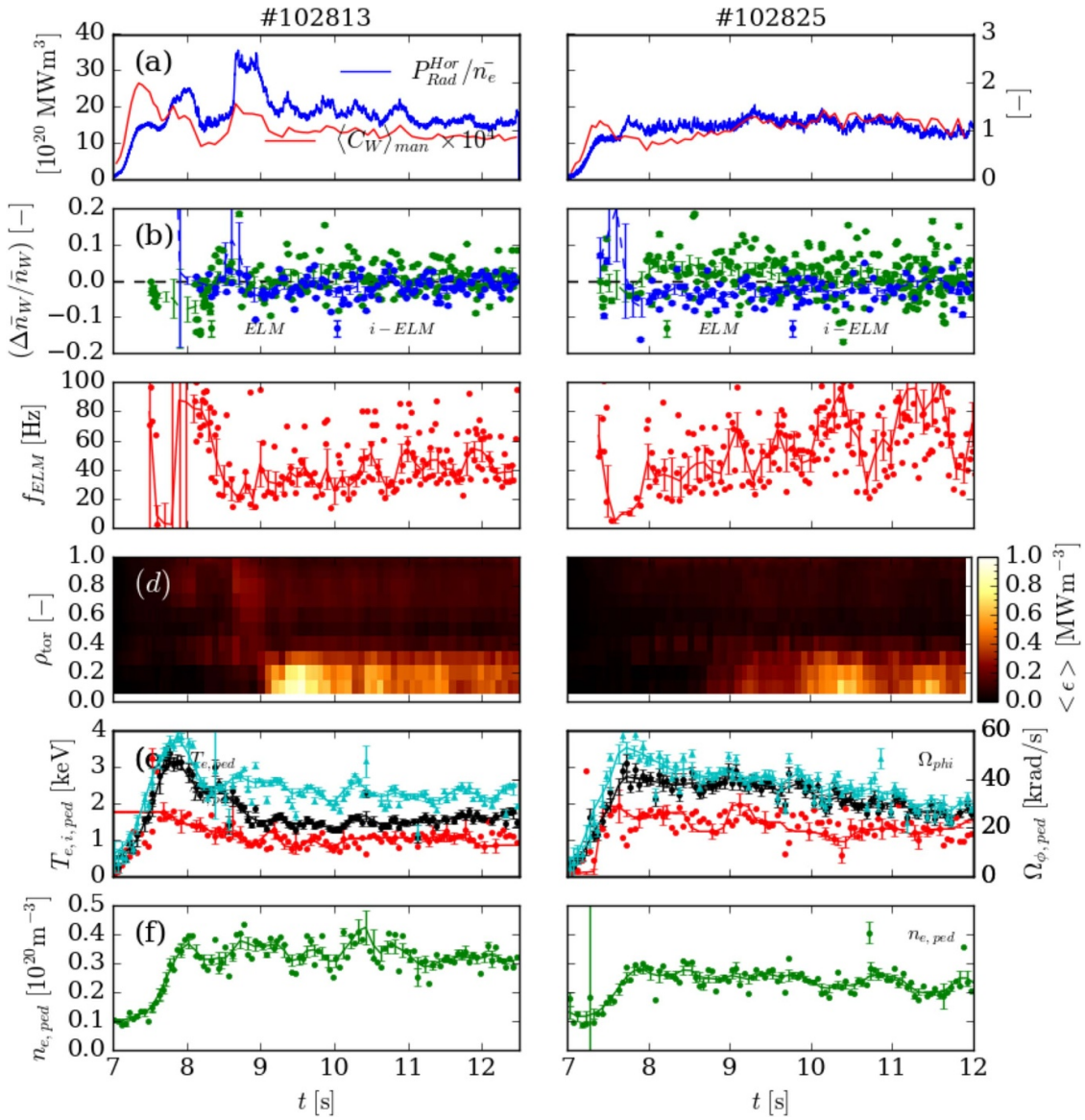

Figure 7. Comparison of the two hybrid-scenario D pulses #102813 (2.3 MA) and #102825 (2.1 MA) showing the evolution of: (*a*) the flushing signal $f_{\rm fl} = P^{\rm Pl}_{\rm Rad}/\bar{n}_{\rm e}$ (blue) and the mean W concentration over the 'mantle' region $\langle C_{\rm W}\rangle_{\rm man}$ (red); (*b*) relative changes in the W content of the confined plasma due to ELMs $(\Delta\bar{n}_{\rm W}/\bar{n}_{\rm W})_{\rm ELM}$ (•) and during the inter-ELM periods $(\Delta\bar{n}_{\rm W}/\bar{n}_{\rm W})_{\rm i-ELM}$ (•); (*c*) the ELM frequency $f_{\rm ELM} = 1/\Delta t_{\rm ELM}$ (•) and time-averaged values $\langle f_{\rm ELM}\rangle$ (red) ; (*d*) the FSA total emissivity $\langle\epsilon_{\rm tot}\rangle$ as a function of normalised radius $\rho_{\rm tor}$; (*e*) the pedestal electron $T_{\rm e,ped}$ (•) and ion $T_{\rm i,ped}$ (•) temperatures and the toroidal angular velocity at the density pedestal top $\Omega_{\phi\,{\rm i,ped}}$ (•); and (*f*) the pedestal density $n_{\rm e,ped}$ (•).

Average values of the $(\Delta\bar{n}_{\rm W}/\bar{n}_{\rm W})_{\rm ELM}$ and $(\Delta\bar{n}_{\rm W}/\bar{n}_{\rm W})_{\rm i-ELM}$ data over the steady phase of the two pulses from figure 8 are stated in table 1, from which it can be seen that the lower current 2.1 MA pulse #102825 exhibits significantly stronger W screening behaviour than the higher current 2.3 MA pulse #102813, by a factor ∼2.2 in the average of the $(\Delta\bar{n}_{\rm W}/\bar{n}_{\rm W})_{\rm i-ELM}$ data from the vertical camera with a larger difference by a factor ∼7 in the average changes due to the ELMs $(\Delta\bar{n}_{\rm W}/\bar{n}_{\rm W})_{\rm ELM}$. There are relatively less data points from analysis of the horizontal camera data from pulse #102825 because later in the pulse $f_{\rm ELM}$ often exceeds $f^{\rm max}_{\rm ELM}$.

In both pulses, the vertical camera data shows that, on average, the ELMs allow W back into the confined plasma, i.e. positive values of $(\Delta\bar{n}_{\rm W}/\bar{n}_{\rm W})_{\rm ELM}$, rather than them flushing out the W impurities. However, the data from the horizontal camera shows negative values of $(\Delta\bar{n}_{\rm W}/\bar{n}_{\rm W})_{\rm ELM}$ for pulse #102813, i.e. flushing behaviour, but positive values for pulse #102825, i.e. ELMs allowing W back into the confined plasma.

In the following section 3.5, modelling of the NC W particle transport is used to predict the W density $n_{\rm W}$ and total emissivity $\epsilon_{\rm tot}$ profiles for comparison with bolometry measurements, with the goal of determining the radial region over

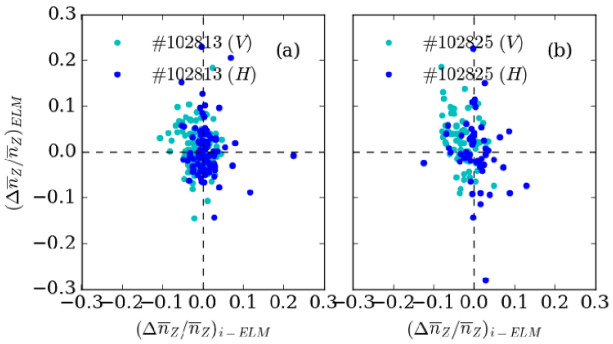

Figure 8. Comparison for the two hybrid-scenario pulses #102813 (2.3 MA) and #102825 (2.1 MA) of the relative changes in the W content of the plasma due to ELM flushing $(\Delta\bar{n}_W/\bar{n}_W)_{ELM}$ vs' the change due to the inter-ELM influx $(\Delta\bar{n}_W/\bar{n}_W)_{i-ELM}$, evaluated over the time periods of $7.5-12.0$ s and $7.5-11.0$ s respectively, using data from either the horizontal (•) or vertical (•) bolometer camera channels shown in figure 4.

Table 1. Relative changes W content per ELM ($(\Delta\bar{n}_W/\bar{n}_W)_{ELM}$) and inter-ELM period ($(\Delta\bar{n}_W/\bar{n}_W)_{i-ELM}$) for the two hybrid pulses shown in figure 7 averaged over the time periods of 8–12 s for pulse #102813 and 8–11 s for pulse #102825.

Pulse	$(\Delta\bar{n}_W/\bar{n}_W)_{ELM}$ [%]		$(\Delta\bar{n}_W/\bar{n}_W)_{i-ELM}$ [%]	
#	H	V	H	V
102813	-1.2 ± 0.4	0.5 ± 0.4	-0.6 ± 0.2	-1.4 ± 0.3
102825	1.5 ± 0.4	3.4 ± 0.4	0.0 ± 0.3	-3.0 ± 0.3

which the temperature-gradient W screening occurs in these pulses.

3.5. Collisional, NC impurity flux

3.5.1. FACIT model of NC impurity transport. For a brief introduction to the NC transport theory underlying the FACIT code the reader is referred to section 3.4.1 of [5] and references therein.

For the core plasma parameters achieved in these high-power hybrid-scenario pulses in JET-Be/W, i.e. relatively low density and high temperature, both the main and impurity ions are in the banana regime. Under these conditions, a more complete treatment of NC theory for arbitrary collisionality regimes is required than the standard PS treatment [28], which applies with collisionless main ions and collisional impurities. In the PS regime, the value of the T_i' screening parameter $C_{TS}=1/2$. The effect of toroidal rotation on impurity transport in the PS regime is treated in [29].

The analytic FACIT model of NC impurity transport described in [30], provides an approximation to results of the drift-kinetic code NEO [31–33], encompassing scans over the relevant parameter space. In this model, the transport coefficients of equation (2) of [30] (D_I^c, K_I^c, H_I^c) are each dependent on the parameters (g,Z_I,A_I,f_t), where $g=qR/(v_{th,i}\tau_{ii})\equiv\nu_{ii}^*\epsilon^{3/2}$ is the collisionality parameter, ν_{ii}^* is the main ion collisionality, τ_{ii} is the self-collision time of the main ions[15] and f_t is the trapped particle fraction.

The FACIT model has now been extended in [9] to incorporate the additional additional dependence of the impurity transport coefficients on toroidal rotation, which affects the transport coefficients by modifying the poloidal distribution of the particle densities, particularly of the heavy impurities such as W. This introduces a further dependence on the toroidal Mach number $M_{\phi,i}$[16] as well as the parameters (g,Z_I,A_I,f_t).

In FACIT, the effect of the poloidal distribution of the plasma potential $\Phi(\rho,\theta)$, which develops in response to the toroidal rotation to maintain parallel force balance on the ions, on the impurity density distribution is accounted for in terms of the generalised Mach number of the impurity ions defined as $M_{\phi,I}^{\star 2}=\left[\frac{A_I}{A_i}-\frac{Z_I}{Z_i}\left(\frac{Z_{eff}}{(Z_{eff}+T_i/T_e)}\right)\right]M_{\phi,i}^2$.

The effect of rotation on the temperature screening parameter $C_{TS}=-H_I/K_I$ (where the coefficients H_I and K_I are sums over components for all collisionality regimes) depends on whether the impurities are in the PS or Banana–Plateau (BP) regime. The magnitude of C_{TS} increases with rotation, both at low collisionality ($g\lesssim10^{-3}$), where $C_{TS}>0$ and T_i' screens the impurities, and at high collisionality ($g\gtrsim1$), where $C_{TS}<0$ and T_i' enhances the impurity pinch.

Note that collisions with fast ions driven by ICRH heating can also modify the poloidal distribution of the impurity densities, even reversing the NBI-driven asymmetry, resulting in a higher impurity density at the HFS in the plasma core where the fast ion density is high [20].

The branch of the FACIT model used here is based on the usual Hinton and Wong ordering of NC transport theory [28], in particular that the parameter $\rho^\star\equiv\rho_{i,\theta}/L_\perp$ (where $\rho_{i,\theta}$ is the ion Larmor radius in the poloidal magnetic field and $L_\perp$ the gradient scale length perpendicular to the flux surfaces) is small, i.e. $\rho^\star<<1$. This *local* model is also not appropriate when the ion–ion collision time τ_{ii} becomes comparable to the characteristic time of parallel flow, i.e. $\tau_{i,\|}\equiv qR/v_{th,i}$. In this situation, the global (non-local) nature of the pedestal can become important.

This is the case when the parameter $g^\star=Z_I^2\rho^\star\tau_{i,\|}/\tau_{ii}$ (referred to here as $g^\star$ to distinguish from the collisionality parameter g defined above) in the papers of Fülöp and Helander [35–37] becomes large, i.e. $g^\star>1$. Under such high-collisionality conditions, poloidal asymmetries in the impurity density can develop and the resulting NC particle flux, which becomes sensitive to the magnetic geometry, can also be strongly reduced.

[15] The self-collision time of the hydrogenic main ions is defined as $\tau_{ii}=\frac{3(2\pi)^{3/2}\epsilon^2\sqrt{m_p}T_i^{3/2}}{n_i e^4\ln\Lambda}$, where m_p is the proton mass and $\ln\Lambda$ is the Coulomb logarithm [34].

[16] The toroidal Mach number of the main ions is defined as $M_{\phi,i}=R\Omega_{\phi,i}/v_{th,i}$, where $\Omega_{\phi,i}$ is the toroidal angular velocity, $v_{th,i}=(2T_i/m_i)^{1/2}$ is the ion thermal velocity, $m_i=A_i m_p$, m_p is the proton mass and $A_i=2$ for D^+ as the main ion species.

Following the derivation of Maget in [38], FACIT also contains a branch in which friction effects on the parallel flow of impurities with that of the main ions are included to the lowest order [39]. This branch of the FACIT model could be used to test the magnitude of such effects. However, it does not contain BP transport, and contains a treatment of PS transport which has not been completely calibrated to reproduce the NEO results in the appropriate limits.

3.5.2. Calculation of the W transport coefficients. Here, the FACIT code, which is based on the analytic model of [9], is used for calculation of the NC transport coefficients for the W impurities $D_{\mathrm{NC},Z}$ and $V_{\mathrm{NC},Z}$. This code is used, rather than the drift-kinetic code NEO [31–33], as was used for the modelling presented in our earlier publication [5], owing to its greater speed compared to that of NEO.

In our implementation, FACIT is coupled to the JETTO [40] transport code, to provide profiles of the required input parameters (n_e, T_e, T_i, $M_{\phi,\mathrm{i}}$, Z_eff and the safety factor q), fitted to the measured raw data and mapped to the magnetic equilibrium. The source and processing of the kinetic profile data is explained in section 3.5.3 below.

3.5.3. Kinetic profile data. An example of the raw and fitted kinetic profile data (n_e, T_e, T_i and $\Omega_{\phi,\mathrm{i}}$) is shown in figure 9 for the pulse #102813, averaged over a 0.5 s period of the post-accumulation phase from $9.0-9.5$ s, where both the raw and fitted data are averaged separately, after performing separate fits to measurements at 50 ms intervals[17].

The raw n_e and T_e data is measured by the high-resolution Thomson scattering (HRTS) system [41] at the laser repetition period of 50 ms and T_i and $\Omega_{\phi,\mathrm{i}}$ by the core [42] and edge [15] charge-exchange-recombination spectroscopy (CXRS) systems observing Ne^{10+} emission lines from a trace Ne impurity with an integration period of 10 ms. Profiles measured during or immediately following ELMs are not included in the set of averaged profiles. Note that there are no CXRS measurements for $\rho_\mathrm{tor} \lesssim 0.35$, so the profiles of T_i and $\Omega_{\phi,\mathrm{i}}$ within this region are only extrapolations of the fitted profiles and hence quite uncertain.

The profiles are fitted using a 3rd-order polynomial over the core and an mtanh() function [43] over the pedestal region, which is constrained to give zero value in the SOL. The low-order function used to fit the core data is the reason why the profiles depart from the measurements in some places. However, this does provide a reasonable interpolation between the measurements from the core and edge CXRS systems, the former typically measuring slightly higher values of T_i than the edge system over the region where the measurements overlap. The influence of weighting the measurements to favour of either the core or edge CXRS T_i data on our modelling results has been investigated and found not to change significantly the results of our NC W transport modelling.

[17] Note that the profiles must be plotted vs' $\rho_\mathrm{pol} \equiv (\psi_\mathrm{N})^{1/2}$ rather than ρ_tor because the toroidal flux is not defined outside the LCFS.

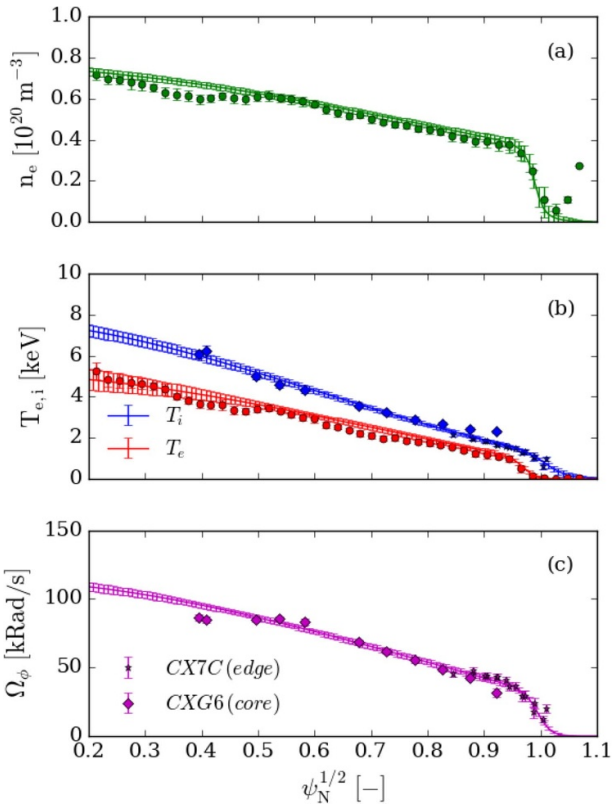

Figure 9. Profiles of n_e (*a*); T_e and T_i (*b*); $\Omega_{\phi,\mathrm{i}}$ (*c*) for the pulse #102813 vs' $\psi_\mathrm{N}^{1/2}$, where ψ_N is the normalised poloidal flux. The fitted profiles (lines) and raw measurement data (points) from HRTS and the core and edge CXRS systems are both separately averaged over the 0.5 s time period $9.0-9.5$ s.

As well as these parameters, the mass numbers of the impurity ($A_\mathrm{I} = m_\mathrm{I}/m_\mathrm{p} = 184$ for W) and main ions ($A_\mathrm{i} = 2$, charge $Z_\mathrm{i} = 1$ for D^+) and the profile of the mean charge state $\bar{Z}$ of the impurity ions are also required. Profiles of $\bar{Z}$ for the W ions, calculated assuming the W impurities are in coronal ionisation equilibrium, in which case $\bar{Z}(n_\mathrm{e}, T_\mathrm{e})$, are obtained from the ADAS Atomic Data Analysis Structure [27, 44]. In these pulses, the mean W charge state $\bar{Z}$ in the plasma core reaches $\mathrm{W}^{\sim 50+}$, while at the pedestal top typical values are in the range W^{20-30+}.

In FACIT, the parameter Z_eff enters into calculation of the effective Mach number $M^\star_{\phi,\mathrm{I}}$, reducing the in–out density asymmetry of the trace high-Z ion species as Z_eff increases. This has the effect of increasing the PS component of the high-Z impurity flux, which is always inwards. In all of the FACIT calculations presented here a Z_eff profile of the form: $Z_\mathrm{eff} = 0.2(1-(r/a)^4) + 1.3$ is assumed, representing a typical profile of the contribution to Z_eff from low-Z ions, e.g. D and Be.

Note that the FACIT calculations are valid for a trace high-Z impurity in a background plasma with low Z-impurities represented by a constant Z_eff on flux surfaces, but is unable to calculate the transport correctly if collisions with mid-Z impurities

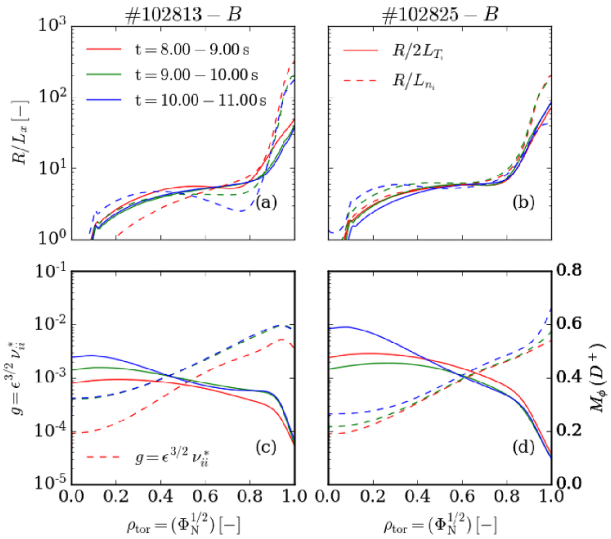

Figure 10. Profiles of parameters input to FACIT vs' normalised radius ρ_{tor} for the two hybrid-scenario pulses #102813 (at 2.3 MA, left) and #102825 (at 2.1 MA, right), showing: (*a*), (*b*) the normalised gradients R/L_{n_i} (dashed) and $R/2L_{T_i}$ (solid); (*c*), (*d*) ion collisionality parameter $g = \epsilon^{3/2}\nu^*_{ii}$ (dashed) and toroidal Mach number of the D^+ ions $M_\phi(D^+)$ (solid), averaged over the three time periods indicated in the legend.

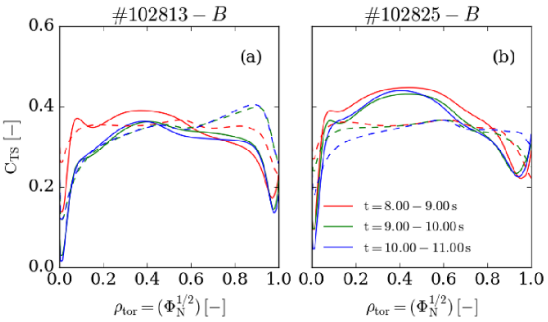

Figure 11. Profiles of the temperature screening parameter C_{TS} vs' normalised radius ρ_{tor}, calculated using FACIT for the two pulses #102813 (left) and #102825 (right) with the input profiles shown in figure 10 for the three time ranges indicated in the figure, showing cases both with rotation ($M_{\phi,i} \neq 0$, solid) and without rotation ($M_{\phi,i} = 0$, dashed).

with an appreciable rotation-driven in–out asymmetry, e.g. Ni, are significant, a point which is discussed further in section 5.

3.5.4. Normalised gradients, $M_{\phi,i}$ and ν^*_{ii} comparison. Profiles of the normalised gradients of the ion density R/L_{n_i} and ion temperature $R/2L_{T_i}$, to which the density and temperature gradient driven impurity fluxes are proportional, are shown averaged over three 1 s time periods in figures 10(*a*) and (*b*) for the two pulses #102813 and #102825. (The factor 1/2 multiplying R/L_{T_i} represents the screening parameter C_{TS} when the impurities are in the collisional PS regime, in which case $R/2L_{T_i} > R/L_{n_i}$ (or equivalently $\eta_i \equiv L_{n_i}/L_{T_i} > 2$) implies an outward NC impurity flux.) Also shown in figures 10(*c*) and (*d*) are profiles of the ion–ion collisionality parameter $g = \epsilon^{3/2}\nu^*_{ii}$ and of the toroidal Mach number of the main D^+ ions $M_{\phi,i}$.

Comparing the profiles between the two pulses, the differences are subtle: in the lower current 2.1 MA pulse #102825, the Mach number $M_{\phi,i}$ is slightly higher and collisionality parameter g is slightly lower ($\sim \times 0.5$) than in the higher current 2.3 MA pulse #102813, both of which favour T_i gradient impurity screening. Just inside the pedestal top[18] at $\rho_{tor} \sim 0.8$, $M_{\phi,i} \sim 0.4$ in pulse #102825, while it is ~0.35 in pulse #102813.

While the normalised temperature profiles $R/2L_{T_i}$ appear very similar between the two pulses, the normalised density density gradient R/L_{n_i} is stronger over the mantle region in the lower current pulse #102825, due to the lower $n_{e,ped}$ than in the higher current pulse #102813. The stronger R/L_{n_i} favours inward W impurity convection rather than T_i' screening over the mantle region of the lower current pulse, hence negating the beneficial effects of the lower collisionality and higher Mach number.

3.5.5. T_i gradient screening parameter C_{TS}. Profiles of the screening parameter C_{TS} calculated using FACIT are shown in figure 11. Cases both with the measured toroidal rotation ($M_{\phi,i} > 0$) and with no rotation ($M_{\phi,i} = 0$) are shown, from which the rotational enhancement of C_{TS}, favouring impurity screening in the low collisionality ($g \lesssim 10^{-3}$) core region is clearly evident. At the higher collisionalities ($g \gtrsim 10^{-2}$) prevailing over the pedestal gradient region the effect of rotation is to decrease C_{TS}, thereby enhancing the inward impurity pinch.

Over the core region, values of C_{TS} approach ~0.5 at mid-radius in the lower current pulse #102825, while being slightly lower ~0.4 in the higher current pulse #102813. Conversely, over the more collisional pedestal gradient region, much lower values of $C_{TS} \sim 0.2$ prevail, thus requiring a larger value of the parameter $\eta_i \gtrsim 5$ to achieve impurity screening across the pedestal than across the core, where $\eta_i \gtrsim 2$ would suffice.

Profiles of the calculated W diffusion coefficient $D_{NC,Z}$ and of the NC convection velocity $V_{NC,Z}$ for the W ions are shown in figure 12 for the pulses #102813 and #102825. Profiles calculated both with and without rotation show that the NBI-driven toroidal rotation enhances the impurity transport by $\gtrsim \mathcal{O}(10)$ above the level for a non-rotating plasma.

The profiles of W diffusivity $D_{NC,Z}$, which is $\sim\mathcal{O}(0.1)\,m^2\,s^{-1}$ at mid-radius, are only subtly different between the two pulses. The NC W convection is predominantly inward ($V_{NC,Z} < 0$) and stronger $\sim\mathcal{O}(20)\,m^2\,s^{-1}$ over the pedestal gradient region and in the deep core, but exhibits stagnation, i.e. $V_{NC,Z} \sim 0$ at mid-radius, where the W transport is purely diffusive. Only in pulse #102813 at the earliest time is the W convection weakly outward ($V_{NC,Z} > 0$) inside mid-radius and also at the later time just inside the pedestal top.

[18] The top of the density pedestal is located at $\rho_{tor} \sim 0.95$.

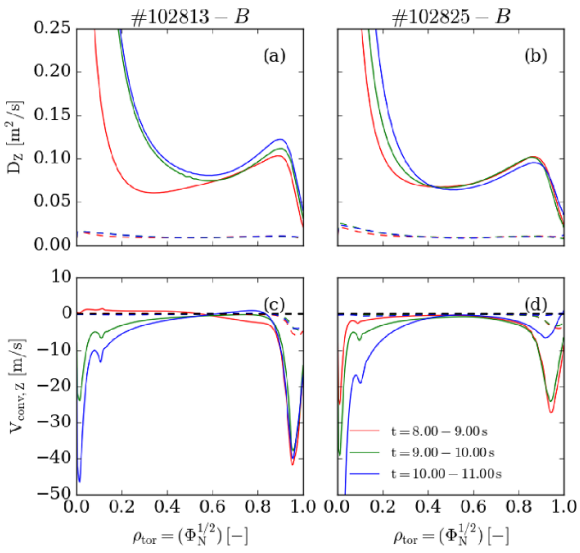

Figure 12. Profiles of the NC transport coefficients for W calculated for the two pulses #102813 (left) and #10825 (right) using FACIT with the input profiles shown in figure 10 for the three time ranges indicated in the figure, showing: (*a*), (*b*) the diffusion coefficient $D_{NC,Z}$; and (*c*), (*d*) the radial convection velocity $V_{NC,Z}$ vs' normalised radius ρ_{tor}.

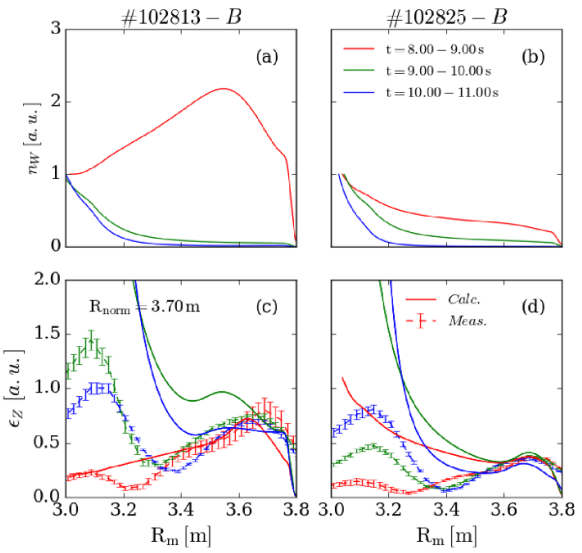

Figure 13. Profiles across the LFS mid-plane vs' major radius R_m, of: (*a*), (*b*) the W density n_W (normalised to 1 at the magnetic axis); and (*c*), (*d*) the measured total emissivity from bolometer tomography ϵ_{tot} (dashed) and the calculated total emissivity of W $\epsilon_{tot,W}$ (solid), where the latter is normalised to the former at $R_m = 3.7$ m, for pulses #102813 (left) and #102825 (right) calculated using the transport coefficients from FACIT shown in figure 12.

The resulting values of $D_{NC,Z}$ and $V_{NC,Z}$ can be used to calculate the W density profile, both as a FSA quantity $\langle n_W \rangle$ and across the LFS major radius through the magnetic axis $n_W(R)$, as described in section 3.6 below. These are then used to calculate the total corresponding emissivity profiles of the W impurities, which are then compared with the measured total emissivity from bolometry.

3.6. W density and emissivity profiles

3.6.1. Calculation of the W density and emissivity profiles with measurments. Profiles of the density and the total emissivity of the W impurities, both at the LFS mid-plane as a function of major radius R and FSA values as a function of normalised radius ρ_{tor}, are calculated in the same way as described in section 3.6 of [5], which follows that of [45].

For calculation of the anomalous turbulent impurity diffusivity $D_{an,W}$, this is assumed to be equal to that of the background D^+ ions D_{an}, where an expression for mixed Bohm/gyro-Bohm transport is used [46], which is computed with the JETTO transport code [47]. Calculated values of the Bohm/gyro-Bohm diffusivity D_{an} are $\lesssim 0.5\,m^2\,s^{-1}$ across most of the plasma radius, increasing to $\lesssim 1.5\,m^2\,s^{-1}$ across the pedestal gradient region[19].

Profiles of the W density across the LFS mid-plane $n_W(R, \theta = 0)$ for the two pulses #102813 and #102825 are shown in figures 13(*a*) and (*b*) for the times indicated in the figure, from which it can be seen that the profiles are peaked, except for the earliest time in pulse #102813, when $V_{NC,Z}$ is positive inside $\rho_{tor} \sim 0.6$, resulting in the W density peaking at this location.

Note that here, n_W is strongly increasing inwards across the pedestal gradient region, consistent with the strong inward NC pinch. The FSA W density profiles, shown in figures 14(*a*) and (*b*) exhibit similar features, although for the first profile which peaks at mid-radius at the LFS the FSA profile peaks on-axis instead.

3.6.2. Comparison of emissivity profiles with measurements. Profiles of the measured total emissivity across the LFS mid-plane, determined from tomographic reconstructions of the bolometer data are compared to the calculated emissivity profiles in figure 13 for the two pulses #102813 and #102825. Because only the relative emissivity profiles can be calculated without knowledge of the W influx, the calculated profiles are normalised to the measured values at $R = 3.7$ m. Similarly, the FSA emissivity profiles $\langle \epsilon_{tot} \rangle$ are normalised to the measured profiles from the bolometer tomography $\langle \epsilon_{tot,m} \rangle$ at $\rho_{tor} = 0.7$.

During the first of these time ranges 8.0–9.0 s, the W had not yet accumulated in the core, as evident from the emissivity profiles. For pulse #102813, the agreement of the predicted W emissivity $\epsilon_{tot,W}$ with that measured $\epsilon_{tot,m}$ is good, however, for the other pulse #102825, the predicted profile is rather too peaked. During the later two periods of 9.0–10.0 s and 10.0–11.0 s, the W has partially accumulated in the core.

[19] Note that values of the power balance ion heat diffusivity χ_{eff} from JETTO, which is found to be of roughly similar magnitude to D_{an} from the Bohm/gyro-Bohm model, and assuming a given ratio of D_{an}/χ_{eff} could be used to estimate D_{an} instead of using the Bohm/gyro-Bohm values as we have done here.

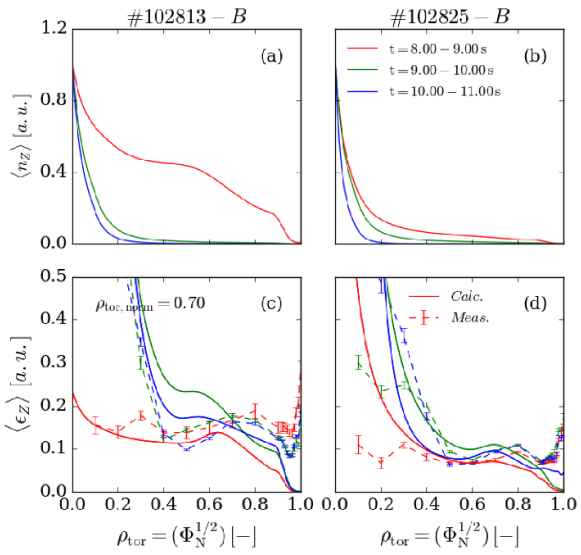

Figure 14. Flux-surface-averaged (FSA) profiles vs' $\rho_{\rm tor}$ of: (*a*), (*b*) the W density $\langle n_{\rm W}\rangle$ (normalised to 1 at $\rho_{\rm tor}=0$); and (*c*), (*d*) the total emissivity $\langle \epsilon_{\rm tot}\rangle$ from bolometer tomography and the calculated total emissivity of W $\langle \epsilon_{\rm tot,W}\rangle$ (where the latter is normalised to the former at $\rho_{\rm tor}=0.7$), for pulses #102813 (left) and #102825 (right), calculated using the transport coefficients from FACIT shown in figure 12.

The predicted profiles from FACIT tend to over predict the degree of core accumulation during these later times, which could be explicable if the assumed values of the anomalous particle diffusivity $D_{\rm an}$ were too low. For example, an enhancement of $D_{\rm an}$ due to the localised ICRH heating of the core plasma is not accounted for in the calculated Bohm/gyro-Bohm values. Another possible reason for the over-prediction of the central peaking is that there are large uncertainties of the $T_{\rm i}$ gradient in the core region ($\rho_{\rm tor}<0.35$), where there are no CXRS measurements and the fitted $T_{\rm i}$ profile is an extrapolation.

Outside the separatrix ($R_{\rm sep}\sim 3.81\,$m), $\epsilon_{\rm tot,W}$ is not calculated, while the measured profile may be broadened somewhat into the SOL due to the finite spatial resolution ($\delta R\sim 0.05-0.1\,$m) of the bolometric measurements and the tomographic reconstruction. There is certainly no hollowness of the measured emissivity across the pedestal gradient region, as is evident in the FSA emissivity profiles shown in figure 14.

The FSA emissivity profiles $\langle \epsilon_{\rm tot}\rangle$ in figure 14 show that the radiation from the mantle region is less significant in a FSA sense compared to that from the LFS mid-plane, where the W is localised by the toroidal rotation. However, the larger volume of this region compared to the core ($\rho_{\rm tor}<0.4$) results in $\sim$40% of the radiated power being emitted from impurities in the mantle, while only $\sim$30% is emitted from the core.

Note that the hollowness of the measured $\langle \epsilon_{\rm tot}\rangle$ profiles over the pedestal gradient region, which might be a result of spill-over of emission from the HFS divertor region, is not reproduced by the calculated profiles. Although FSA data is not available outside of the separatrix ($r/a>1$), the LFS profiles in figure 13 show that there is significant emission from impurities the SOL region. The 2D distributions in figure 4 show that the radiation from the pedestal foot and SOL is dominated by emission from the region above the HFS divertor leg.

In experiments with N_2 seeding in ASDEX-U, such emission from the so-called HFS high-density region has been attributed to hydrogenic emission from the detached inner divertor leg [48]. However, in the high-power, hybrid scenario pulses discussed here, the divertor is not detached.

Measurements of W influxes at the divertor targets using visible spectroscopy [49] on JET-Be/W have shown the source of sputtered W from the inner divertor to be significant, so appreciable W emission from this region is to be expected. Unfortunately, there were no vacuum-ultra-violet (VUV) spectroscopic measurements of the inner divertor region, which would be required to quantify this w emission.

3.7. Discussion of the effect of reduced plasma current

Here, the main results of our analysis and modelling comparing the two high-power, hybrid pulses #102813 and #102825 with plasma currents of 2.3 MA and 2.1 MA respectively, both with 3.45 T toroidal field, are summarised and compared with those from the earlier optimised hybrid pulse #97781 of [5].

The primary effect of reducing the plasma current from 2.3 MA to 2.1 MA is to decrease $n_{\rm e,ped}$ by $\sim$30% and to similarly increase $T_{\rm i,ped}$, as was intended, with the aim of increasing the peripheral W screening by steepening the $T_{\rm i}$ gradient across the pedestal. Indeed, as shown in figure 8, results of analysis of the bolometry data do show increased W screening, i.e. more negative $(\Delta\bar{n}_{\rm W}/\bar{n}_{\rm W})_{\rm i-ELM}$ by a factor $\sim\times 2$, in the lower current pulse (see table 1). Consequently, the radiated power fraction $\mathcal{F}_{\rm Rad}^{\rm Pl}$ is significantly lower (by $\sim$40%), although this is at least in part due to the lower density of the lower current pulse.

Our approximate estimates of the NC convection parameter $\zeta_{\rm NC}$, show that initially, during over-shoot phase high $T_{\rm i}$ gradient across core is sufficient for the resulting outward NC convection to screen out the W impurities from the core, localising them to the mantle region. From there, the ELMs can flush them out of the confined plasma, as is seen in the $(\Delta\bar{n}_{\rm W}/\bar{n}_{\rm W})_{\rm ELM}$ data from early in the pulse (8.5 s), at least for pulse #102813. This initial outward NC convection across the core is also reproduced by the more rigorous W transport modelling using FACIT, as seen in figure 14.

Later in the pulses, after the core ITB is lost, the $T_{\rm i}$ gradient is insufficient to screen the W impurities from the core. At mid-radius, the NC W convection predicted using FACIT is very weak ($V_{\rm NC,Z}\sim 0\,{\rm m\,s^{-1}}$), but more negative further into the core, so the accumulation is partial with significant W remaining in the outer mantle region. The reasonable agreement between the calculated W emissivity and the total emissivity from the bolometer tomography, particularly for the FSA profiles shown in figure 14, lends credence to our FACIT calculations of the W transport.

In spite of the bolometry analysis showing inter-ELM W screening behaviour, i.e. $(\Delta\bar{n}_{\rm W}/\bar{n}_{\rm W})_{\rm i-ELM}<0$, the NC convection across the pedestal gradient region predicted using FACIT is always strongly inwards ($V_{\rm NC,Z}<<0$), which is contrary to this observation. The lower $n_{\rm e,ped}$ and higher $T_{\rm i,ped}$ in

the lower current pulse #102825 does result in a significant reduction in $V_{\mathrm{NC},Z}$, to $\sim -25\,\mathrm{m\,s^{-1}}$ from the $\sim -40\,\mathrm{m\,s^{-1}}$ in the higher current pulse #102813 but is insufficient to reverse the convection.

The effect of reducing I_p and hence $n_{\mathrm{e,ped}}$ in pulse #102825 is to steepen R/L_{n_e} across the mantle region, which runs contrary to inducing NC screening. However, the reduced $n_{\mathrm{e,ped}}$ results in significantly lower collisionality ν^*_{ii} in the periphery of the lower current pulse and the higher rotation $\Omega_{\phi,\mathrm{i}}$ also increases the Mach number $M_{\phi,\mathrm{i}}$. Both of these changes enhance NC screening and counteract the effect of the increased R/L_{n_e}, resulting in similar NC convection across the mantle region in the two pulses.

Unlike in the earlier, optimised hybrid-scenario pulse #97781 discussed in [5], no region of outward NC convection just inside the pedestal top is predicted by the FACIT modelling for either of the pulses discussed here.

The main reason for this difference between the two 2.3 MA pulses #97781 and #102813, which have comparable heating power, is that the normalised T_i gradient R/L_{T_i} is less steep over the region just inside the pedestal top ($0.8 < \rho_{\mathrm{tor}} < 0.95$) in pulse #102813 than in pulse #97781, while the density gradients R/L_{n_i} are similar.

Also, pulse #102813 has slightly higher collisionality and lower Mach number over the mantle region than in pulse #97781, which are both less favourable for impurity screening, rotation slightly increasing the screening parameter C_{TS} in pulse #97781 and decreasing it in pulse #102813.

Possible reasons why the calculations of the NC W transport run contrary to our observation of inter-ELM W screening based on analysis of the bolometer data are discussed in section 5.

4. Comparison of matched 'hybrid' pulses in D and DT

The development of hybrid-scenario plasmas in DT during DTE3 is described in detail in [12]. Previous hybrid-scenario development during DTE2 had used the main chamber TIM-15 for T_2 injection and the faster standard gas injection modules (GIMs) to inject D_2 during the main phase. As explained above in section 3.4, the use of TIM-15 during the main phase compromised the data from the horizontal viewing bolometer camera.

For this reason, hybrid development for DTE3 aimed to use the main chamber TIM-15 only during the pre-heat phase of the pulse and fuel only with the divertor TIM (TIM-10) during the subsequent main phase, while the faster GIMs (GIM-1, 4 and 6) were used to inject D_2 to trigger the first ELM. As this large injection of D_2 and the use of D^0 only beams during DTE3, rather than mixed D^0 and T^0 beams during DTE2, would increase the D:T ratio during the pulse, it was decided instead to start the pulse with all T_2 gas fuelling. Further tuning of the initial gas fuelling was required to avoid hollow temperature profiles and to achieve the optimal target q-profile, which were both achieved by running Ohmic plasmas in both T and DT.

The lower L/H-threshold power P_{LH} in DT plasmas resulted in an earlier H-mode entry and faster initial density ramp, which had to be compensated by reducing P_{NBI} during the initial heating ramp, contrary to the goal of achieving an initially hot pedestal. Hence, it was decided instead to increase P_{LH} by increasing the toroidal field from 3.45 T to 3.85 T, so that the power could be maintained at a higher level during the heating ramp.

With the main-chamber TIM-15 used during the initial phase of the pulse, there was still some detrimental effect on the bolometer camera data, so it was decided to use the divertor TIM-10 for T_2 injection throughout the pulse. The evolution of the resulting hybrid-scenario 2.1 MA/3.85 T DT pulse #104681 is shown in figure 15. The core temperature $T_{\mathrm{i},0}$ was not as high during the overshoot phase as in earlier attempts with 2.45 T toroidal field, however, the pulse did exhibit the highest pedestal ion temperature $T_{\mathrm{i,ped}} \lesssim 3.5\,\mathrm{keV}$. This pulse also suffered from larger than usual influx of mid-Z impurities, in particular titanium, as diagnosed from VUV spectroscopy [50].

Following the DTE3 campaign, further D reference hybrid-scenario plasmas were run at 3.85 T. This was done after the tritium removal phase of the campaign, resulting in a relatively low level of low and medium-Z impurities. The D pulse #105508 at 2.1 MA/3.85 T, shown in figure 15, has the same engineering parameters as the DT pulse #104681 and a matched density rise, with a slightly earlier first ELM.

4.1. Comparison of plasma start-up and evolution

A comparison of the evolution of the two 2.1 MA/3.85 T hybrid scenario pulses #104681 in DT and #105508 in D is shown in figure 15. The total heating power is shown in figure 15(*a*), with the majority from NBI $P_{\mathrm{NBI}} \lesssim 32\,\mathrm{MW}$ and an additional $P_{\mathrm{RF}} \sim 3\,\mathrm{MW}$ and $\sim$1 MW from on-axis H^+ minority ICRH heating in pulses #104681 and #105508 respectively.

The demand waveform for the total hydrogenic fuelling rate $\Gamma_{\mathrm{e}^-}\,[\mathrm{s^{-1}}]$, shown in figure 15(*b*), shows that the gas 'slug' that stimulates the first ELM is $\sim$250 ms later in the DT pulse #104681 and $\sim \times 2$ larger in amplitude than in the D pulse #105508, while the rate during the sustained phase of $1.4 \rightarrow 1.2\,\mathrm{e^{-1}\,s^{-1}}$ in the DT pulse is also about $\sim$40% higher than that in the D pulse.

The radiated power from the confined plasma $P^{\mathrm{Pl}}_{\mathrm{Rad}}$, shown in figure 15(*c*), is similar in the two pulses at $\sim 5-7\,\mathrm{MW}$, representing a radiated power fraction $\mathcal{F}^{\mathrm{Pl}}_{\mathrm{Rad}} \sim 20\% - 30\%$. In the D pulse #105508, both $P^{\mathrm{Pl}}_{\mathrm{Rad}}$ and $\mathcal{F}^{\mathrm{Pl}}_{\mathrm{Rad}}$ increase slightly during the sustained phase, proportionally to the gradually increasing density $\bar{n}_\mathrm{e}$, while in the DT pulse #104681 $P^{\mathrm{Pl}}_{\mathrm{Rad}}$ and $\mathcal{F}^{\mathrm{Pl}}_{\mathrm{Rad}}$ both remain quite constant, as does $\bar{n}_\mathrm{e}$. As shown in figure 15(*e*), $\bar{n}_\mathrm{e}$ is initially $\sim 0.5 \times 10^{20}\,\mathrm{m^{-3}}$ in both pulses and the pedestal density $n_{\mathrm{e,ped}} \sim 0.3 \times 10^{20}\,\mathrm{m^{-3}}$.

During the sustained phase, the stored energy $W_{\mathrm{pl}} \sim 7\,\mathrm{MJ}$ (determined from magnetic equilibrium reconstructions), shown in figure 15(*d*) is remarkably similar in the two pulses. Initially, W_{pl} is higher ($\sim$10 MJ) during the initial over-swing phase of the DT pulse #104681 than in the D pulse #105508

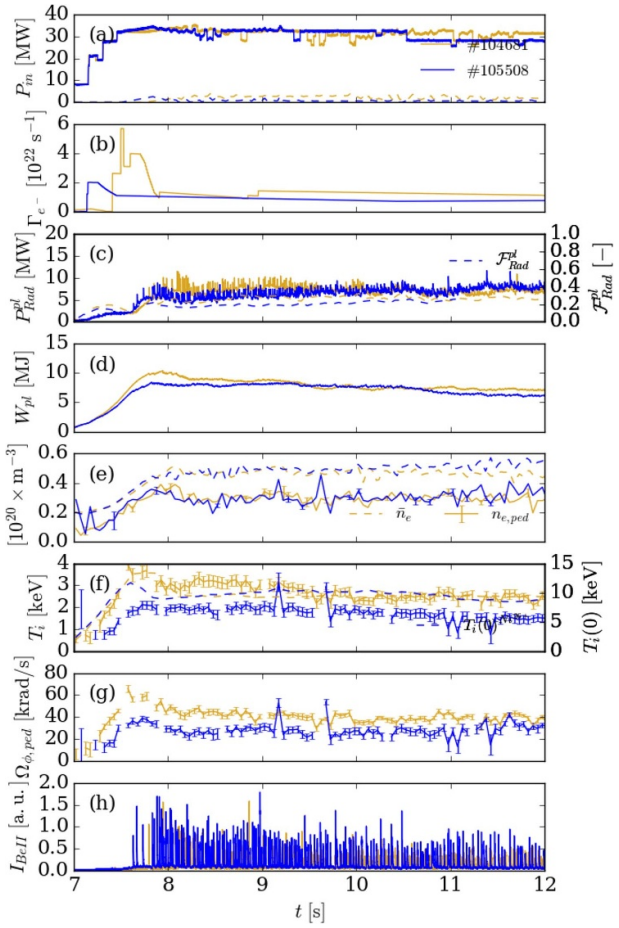

Figure 15. Comparison of the evolution of two, matched 2.3 MA/3.85 T hybrid-scenario pulses #104681 in DT (gold) and #105508 in D (blue), showing the same parameters as in figure 1.

(∼8.5 MJ), which does not exhibit a pronounced initial ITB. Later, in both pulses there is a slight (∼20%) degradation of $W_{\rm pl}$ due to MHD activity after ∼10.5 s in pulse #105508 and ∼1 s earlier in pulse #104681.

The ion temperature, both on axis and at the pedestal top, peaks during the over-shoot phase at ∼7.5 s, when these are $T_{\rm i,0} \sim 14$ keV and $T_{\rm i,ped} \sim 3$ keV in the DT pulse #104681 and ∼11 keV and ∼2 keV respectively in the D pulse #105508. After the over-shoot phase, $T_{\rm i,ped}$ decreases to ∼2 keV in the DT pulse and ∼1.5 keV in the D pulse.

Similarly, the angular velocity at the pedestal top $\Omega_{\phi\,\rm i,ped}$ peaks during the over-shoot phase at ∼60 krad s^{-1} in the DT pulse and ∼40 krad s^{-1} in the D pulse, thereafter remaining quite constant at ∼40 krad s^{-1} in the DT and ∼30 krad s^{-1} in the D pulse.

4.2. Total radiation distribution

A comparison of the 2D distribution of the total emissivity $\epsilon_{\rm tot}(R,Z)$ from tomographic reconstructions of bolometric data for the DT pulse #104681 and the D pulse #105508 at 8.5 s is shown in figure 16. At this time, about 1 s after the initial ITB formation, there is little sign of impurity accumulation at the magnetic axis, while the bright crescent of emission on

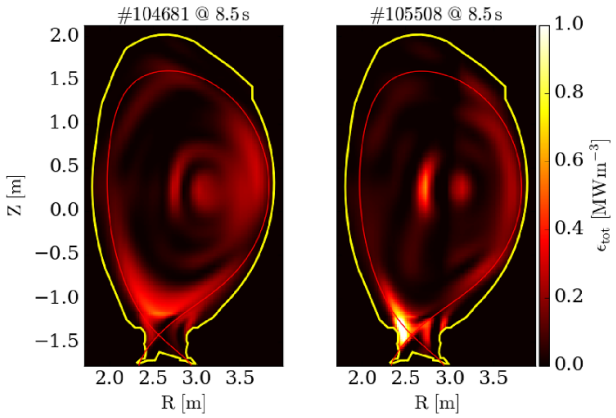

Figure 16. Comparison of the emissivity distribution $\epsilon_{\rm tot}(R,Z)$ from bolometer tomography for the two, matched 2.3 MA/3.85 T hybrid-scenario pulses #104681 in DT (left) and #105508 in D (right) at 8.5 s.

the HFS just inboard of the magnetic axis might be due to an ICRH driven impurity density asymmetry, which can occur when there is sufficient temperature anisotropy ($T_\perp > T_\parallel$) of the minority H^+ ions [20, 51]. The crescent of emission at the LFS mid-plane can be attributed to the in/out asymmetry of emission from W impurities due to the strong rotation [52].

The bright emission at the lower HFS divertor region is more intense in the D pulse #105508 than in either of the two D pulses shown earlier in figure 4, while the overall level of emissivity is lower. In the DT pulse, there is still strong emission from the lower HFS region but this is localised inside the separatrix rather than in the SOL in the vicinity of the inner divertor.

4.3. Evolution of total emissivity profile

As in the previous section 3.2, here simplified proxies for the FSA W density $\langle n_{\rm W}\rangle^\star$ derived from the FSA total radiated emissivity $\langle\epsilon_{\rm tot}\rangle$ and for the NC W convection, which is proportional to the parameter $\zeta_{\rm NC}$, are used to investigate the behaviour of the W impurities over the core plasma.

The evolution of the FSA total emissivity profile $\langle\epsilon_{\rm tot}\rangle$ for the two pulses #104681 and #105508 is shown in figure 18(*d*). As explained in section 3.2 above, under the assumption that W dominates the total emissivity $\epsilon_{\rm tot}$ and a constant value for the W emissivity coefficient $\mathcal{R}_\epsilon$, the measured emissivity can be used to calculate a proxy for the FSA W density $\langle n_{\rm W}\rangle^\star$, the evolution of which is shown in figures 17(*a*) and (*b*).

For the DT pulse #104681, which has significant contamination by Ti impurities, the assumption of W dominating the radiated power at all locations is probably invalid. In this pulse, the emission at mid-radius corresponds to the crescent of emission at the HFS in figure 16, which may be from W or Ti. The strong radiation from the mantle region is likely to be from W impurities at the LFS mid-plane. After ∼9.3 s there is some impurity accumulation in the core plasma.

In the D pulse #105508, the total radiated power is lower by ∼50% than in the DT pulse #104681, which was run after a thorough clean-up of the vessel after the DTE3 campaign,

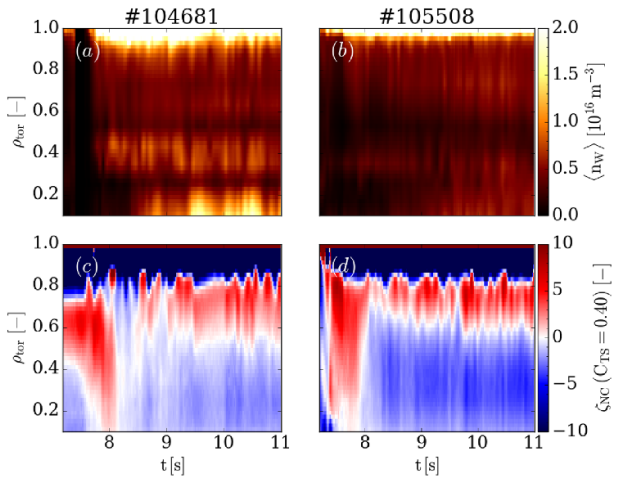

Figure 17. Comparison of the two, matched 2.1 MA/3.85 T hybrid-scenario pulses #104681 in DT (left) and #105508 in D (right) showing the profile evolution of: (*a*), (*b*) a proxy for the FSA W density distribution $\langle n_W \rangle^\star$, where the total emission coefficient is assumed constant; and (*c*), (*d*) a proxy for the NC convection ζ_{NC}, calculated assuming a constant value of the screening parameter $C_{TS} = 0.4$, vs' ρ_{tor}.

resulting in low levels of impurity contamination. There is no significant impurity accumulation in this pulse and the radiation at mid-radius is less evident than in the matching DT pulse.

Initially, in both pulses before ∼8.2 s, the NC convection parameter is positive ($\zeta_{NC} \lesssim 5$) across the outer core plasma. Hence, the impurities are screened from the core plasma during the over-swing phase as a result of the strong T_i gradient from the ITB. For figures 17(*c*) and (*d*), ζ_{NC} is calculated assuming a constant value of the NC screening parameter $C_{TS} = 0.4$. After this initial phase, the NC screening weakens due to the collapse of the ITB and the direction of the NC screening across the core reverses ($\zeta_{NC} < 0$), allowing the impurities to convect inwards across the core plasma.

Calculations with FACIT show that this value of C_{TS} is appropriate for the core plasma ($\rho_{tor} \leqslant 0.6$) but overestimates the screening further outwards, where C_{TS} decreases to ∼0.3 at the pedestal top. Hence, the region of screening ($\zeta_{NC} > 0$) over the mantle region evident during most of the sustained phase in both pulses is not reproduced by detailed calculations of the W transport with the FACIT code, as discussed in section 4.5.

4.4. ELM and inter-ELM W fluences

Our discussion of the quantification of the W content of the confined plasma and relative changes there in $\Delta\bar{n}_W/\bar{n}_W$ due to ELMs and inter-ELM, cross-pedestal W transport follows that of the earlier section 3.4. The flushing signal $f_{fl} = P_{Rad}^{man}/\bar{n}_e$ used to determine $\Delta\bar{n}_W/\bar{n}_W$ and an estimate of the W concentration over the mantle region $\langle C_W \rangle_{man}$ are shown in figure 18(*a*) for the two pulses #104681 (DT) and #105508 (D). For both pulses, $\langle C_W \rangle_{man} \sim 10^{-4}$, with a somewhat lower initial impurity concentration early in the D pulse.

Relative changes in the flushing signal f_{fl}, representing relative changes in the W content due to ELMs ($(\Delta\bar{n}_W/\bar{n}_W)_{ELM}$) and inter-ELM, cross-pedestal transport ($(\Delta\bar{n}_W/\bar{n}_W)_{i-ELM}$) are shown in figure 18(*b*). The same data from the sustained phase of the two pulses is also shown in figure 19 in a different representation, which better illustrates either the inter-ELM W screening (−ve on *x*-axis) or ELM W flushing (−ve on *y*-axis) behaviour.

On average, the $\Delta\bar{n}_W/\bar{n}_W$ data (see table 2) derived from the horizontal bolometer camera (KB5H) data shows a positive (inward) inter-ELM influx $(\Delta\bar{n}_W/\bar{n}_W)_{i-ELM} \sim 3.4 \pm 0.3\%$ the DT pulse, while the D pulse exhibits 'neutral' behaviour $(\Delta\bar{n}_W/\bar{n}_W)_{i-ELM} \sim 0.2 \pm 0.4\%$, i.e. neither clear flushing or screening. However, for the reasons explained earlier in section 3.4, there are reasons to suspect results from analysis of the horizontal camera data.

Using the data from the vertical bolometer camera (KB5V), from which the results are expected to be more reliable, yields for the DT pulse #104681 an average negative value for $(\Delta\bar{n}_W/\bar{n}_W)_{ELM} \sim -1.3 \pm 0.4\%$ and a negative value of $(\Delta\bar{n}_W/\bar{n}_W)_{i-ELM} \sim -0.3 \pm 0.3\%$, i.e. significantly more W flushing by the ELMs than inter-ELM screening behaviour. For the D pulse #105508, the inter-ELM W screening behaviour is more clearly evident, with statistically significant values of $(\Delta\bar{n}_W/\bar{n}_W)_{i-ELM} \sim -2.9 \pm 0.4\%$, while the ELMs cause significant increases $(\Delta\bar{n}_W/\bar{n}_W)_{ELM} \sim 2.6 \pm 0.5\%$ of the W content of the confined plasma.

The ELM frequencies, shown in figure 19(*c*), vary between $40 \lesssim f_{ELM} \lesssim 70$ Hz, which, as discussed in section 3.4, is below the $f_{ELM}^{max} \sim 70$ Hz above which the flushing/screening analysis is invalid hence any results are excluded from plots or averages. Later on in the D pulse #105508, after 9 s when f_{ELM} is lower, the amplitude of the $\Delta\bar{n}_W/\bar{n}_W$ data shown in figure 19(*b*) is larger, i.e. showing more clearly an impurity influx due to the ELMs and screening behaviour during the inter-ELM periods.

The pedestal temperatures, $T_{i,ped}$, $T_{e,ped}$ and toroidal angular velocity at the density pedestal top $\Omega_{\phi i,ped}$, are shown in figure 19(*e*), while the pedestal density n_e is shown in figure 19(*f*), for the two pulses #104681 and #105508.

In the DT pulse #104681, during the over-swing phase prior to 9.5 s, $T_{i,ped}$ and $\Omega_{\phi i,ped}$ are both initially higher than during the sustained phase, reaching ∼3.5 keV and ∼50 krad s^{-1} respectively, while the D pulse #105508 does not exhibit appreciably higher initial values. Later, during the sustained phase $T_{e,ped} \sim 1.5$ keV and $n_{e,ped} \sim 0.3 \times 10^{20}$ m^{-3} are very similar in both pulses, while in the DT pulse, both $T_{i,ped} \sim 2.5$ keV and $\Omega_{\phi i,ped} \sim 40$ kHz are higher than in the D pulse, where $T_{i,ped} \sim 2$ keV and $\Omega_{\phi i,ped} \sim 30$ kHz.

4.5. Results of W transport calculations using FACIT

Data preparation and calculations of the W density n_W and total emissivity $\epsilon_{tot,W}$ profiles using the FACIT code [9] follow the same methodology as described in section 3.6 above, so only the results of these calculations for the D and DT pulses #104681 and #105508 will be described below.

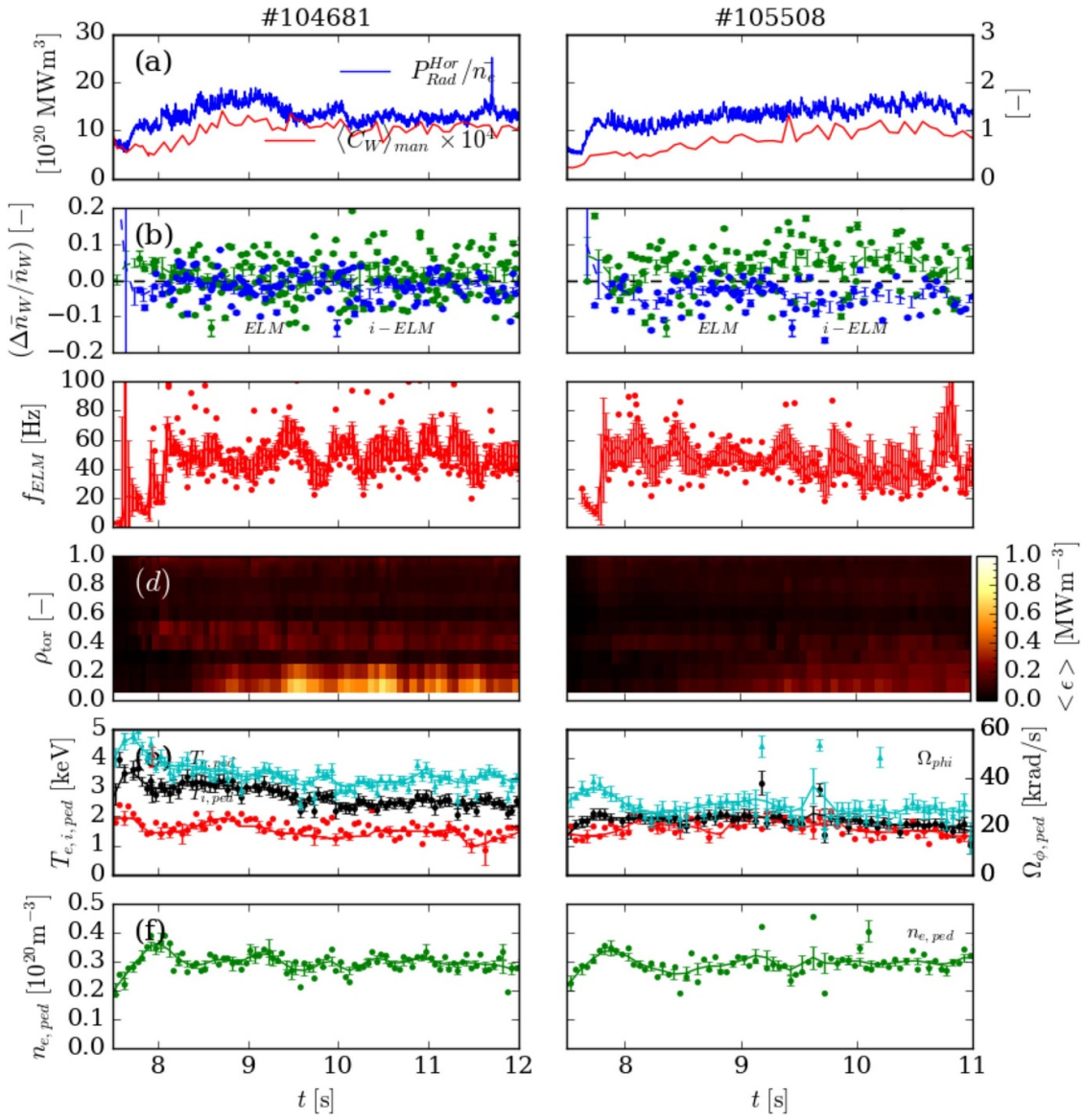

Figure 18. Evolution of the two, matched 2.1 MA/3.85 T hybrid-scenario pulses #104681 in DT (left) and #105508 in D (right) showing: (*a*) the flushing signal $f_{\rm fl}$ (blue) and the mean W concentration over the 'mantle' region $\langle C_{\rm W}\rangle_{\rm man}$ (red); (*b*) relative changes in the W content of the confined plasma $\Delta\bar{n}_{\rm W}/\bar{n}_{\rm W}$ due to ELMs (•) and during the inter-ELM periods (•); (*c*) the ELM frequency $f_{\rm ELM} = 1/\Delta t_{\rm ELM}$ (•) and time-averaged values $\langle f_{\rm ELM}\rangle$ (red); (*d*) the FSA total emissivity $\langle \epsilon_{\rm tot}\rangle$ as a function of normalised radius $\rho_{\rm tor}$; (*e*) the toroidal rotation at the density pedestal top $\Omega_{\phi\,{\rm i,ped}}$ (•) and the pedestal temperatures $T_{\rm e,ped}$ (•) and $T_{\rm i,ped}$ (•); and (*f*) the pedestal density $n_{\rm e,ped}$ (•).

4.5.1. Input profiles. Input profiles to the FACIT calculations of the NC transport coefficients are shown in figure 20. For the DT pulse #104681, the normalised $T_{\rm i}$ gradient is about twice as strong as the $n_{\rm i}$ gradient ($R/2L_{T_{\rm i}} \sim R/L_{n_{\rm i}}$) across most of the plasma radius, i.e. $\eta_{\rm i} \sim 2$. For the D pulse #105508, over the core plasma for $\rho_{\rm tor} \lesssim 0.6$, $R/2L_{T_{\rm i}} < R/L_{n_{\rm i}}$ and $\eta_{\rm i} < 2$, while over the region just inside the pedestal top ($0.6 \lesssim \rho_{\rm tor} \lesssim 0.8$), $R/2L_{T_{\rm i}} > R/L_{n_{\rm i}}$ and $\eta_{\rm i} > 2$.

The collisionality parameter $g = \epsilon^{3/2}\nu^*_{\rm ii}$ for the two pulses are similar across the full profile, ranging from $g = 10^{-4}$ in the core to 10^{-2} in the pedestal gradient region, with somewhat lower values at mid radius in the D pulse than in the DT pulse. The toroidal Mach number $M_{\phi,{\rm i}} \lesssim 0.5$ of the D pulse is slightly higher in the core than in the DT pulse ($\lesssim 0.4$), with similar values ($\sim$0.35) for the two pulses at the pedestal top.

4.5.2. $T_{\rm i}$-gradient screening parameter. Profiles of the $T_{\rm i}$ gradient screening parameter $C_{\rm TS}$, calculated with and without toroidal rotation, for the two pulses are shown in figure 21. The lower collisionality and higher Mach number in the core of the D pulse #105508 favours screening with higher values of $C_{\rm TS} \lesssim 0.4$ than in the DT pulse ($\lesssim 0.35$) #104681. While rotation enhances the W impurity screening in the core of the D pulse, it also increases the inward pinch in at the higher collisionality prevailing in the pedestal gradient region. Just inside

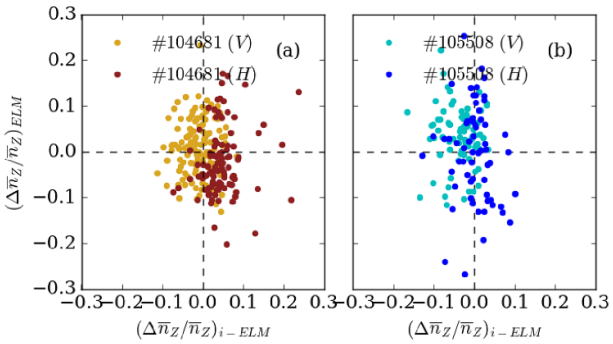

Figure 19. A comparison of the relative changes in the W content of the plasma due to ELM flushing $(\Delta\bar{n}_W/\bar{n}_W)_{ELM}$ vs' the change due to the inter-ELM influx $(\Delta\bar{n}_W/\bar{n}_W)_{i-ELM}$ for the two, matched 2.1 MA/3.85 T hybrid-scenario pulses #104681 in DT (left) and #105508 in D (right) for the time periods $8.0-12.0$ s and $8.0-11.0$ s respectively, using data from either the horizontal (●/●) or vertical (●/●) bolometer camera channels.

Table 2. Relative changes W content per ELM ($(\Delta\bar{n}_W/\bar{n}_W)_{ELM}$) and inter-ELM period ($(\Delta\bar{n}_W/\bar{n}_W)_{i-ELM}$) for the two hybrid pulses shown in figure 7 averaged over the time periods of 8–12 s for pulse #104681 and 8–11 s for pulse #105508.

Pulse	$(\Delta\bar{n}_W/\bar{n}_W)_{ELM}$ [%]		$(\Delta\bar{n}_W/\bar{n}_W)_{i-ELM}$ [%]	
#	H	V	H	V
104681	-3.1 ± 0.4	-1.3 ± 0.4	3.4 ± 0.3	-0.3 ± 0.3
105508	3.6 ± 0.8	2.6 ± 0.5	0.2 ± 0.4	-2.9 ± 0.4

the pedestal top ($\rho_{tor}\sim0.8$), the effect of rotation is to reduce W screening in the DT pulse but has a neutral effect in the D pulse.

4.5.3. NC W transport coefficients. Profiles of the NC transport coefficients $D_{NC,Z}$ and $V_{NC,Z}$ for the W impurities are shown in figure 22 are broadly similar for the two pulses #104681 and #105508. The diffusion coefficient has a shallow minimum $D_{NC,Z}\sim0.07\,m^2\,s^{-1}$ at mid-radius and is higher at the pedestal top and in the core. The radial W convection velocity is mainly inwards $V_{NC,Z}<0$, most strongly across the pedestal gradient region ($\gtrsim-30\,m\,s^{-1}$). However, in the DT pulse, during the earlier time range ($8-9$ s), the convection is slightly positive ($\lesssim1\,m\,s^{-1}$) across the core, and also slightly positive near the pedestal top ($0.6\lesssim\rho_{tor}\lesssim0.8$) for the later times ($9-11$ s) in the D pulse.

4.5.4. W density and emissivity profiles. Predicted profiles of W impurity density n_W and total emissivity $\epsilon_{tot,W}$, calculated using the transport coefficients of figure 22, along with the $\epsilon_{tot,m}$ profiles from bolometric measurements, are shown for the two pulses #104681 and #105508 in figure 23 as a function of major radius R_m across the LFS mid-plane.

In the DT pulse #104681, the weak convection across most of the profile results in n_W profiles that are quite flat over the outer two thirds of the plasma radius, with the weakly positive

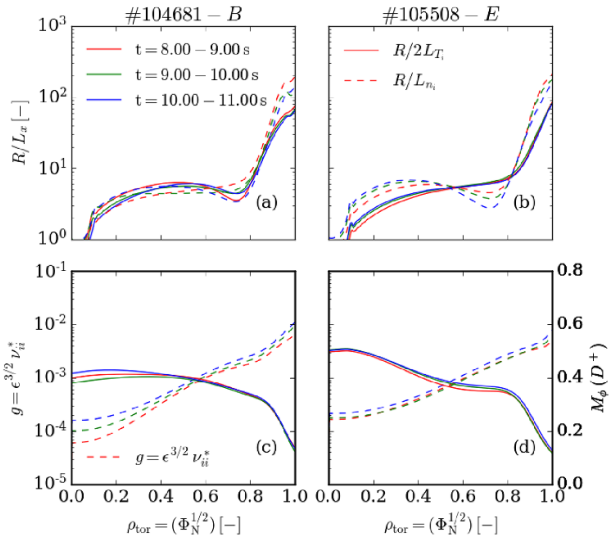

Figure 20. Profiles of parameters input to FACIT vs' normalised radius ρ_{tor} for the two, matched 2.1 MA/3.85 T hybrid-scenario pulses #104681 in DT (left) and #105508 in D (right), showing: (*a*), (*b*) the normalised gradients R/L_{n_i} (dashed) and $R/2L_{T_i}$ (solid); (*c*), (*d*) ion collisionality parameter $g=\epsilon^{3/2}\nu^*_{ii}$ (dashed) and toroidal Mach number of the D^+ ions $M_\phi(D^+)$ (solid), averaged over the three time periods indicated in the legend. Note that for the DT pulse, the effective relative isotope mass of the DT mixture of $A_{eff}\sim2.74$[20] is used for calculation of M_ϕ.

convection at during earliest time resulting in a slightly hollow core profile. At later times, inward convection in the very core ($\rho_{tor}\lesssim0.2$) results in W accumulation, which is seen in the ϵ_{tot} data from the bolometric reconstructions.

In the D pulse #105508, the slightly more negative convection across the core results in more peaking of n_W profiles, i.e. stronger W accumulation is predicted than in the DT pulse. The measured ϵ_{tot} profile does not exhibit such strong peaking as that predicted, i.e. the W accumulation is over predicted for the D pulse during all three time periods shown. Again, we emphasise that there are no CXRS T_i measurements for $\rho_{tor}\lesssim0.35$, so the predicted profiles are not to be relied upon in the very core. Also, any enhancement of the anomalous particle diffusivity D_{an} due to the on-axis ICRH heating is not taken into account in the modelling.

In both pulses, the strong inward NC W convection across the pedestal gradient region concentrates the W impurities at the pedestal top, i.e. the W density is higher at the pedestal top than at the separatrix. Limitation of the spatial resolution of the bolometric measurements and the tomographic reconstructions of ϵ_{tot} prevents confirmation of this prediction.

Equivalent, FSA-averaged profiles of the predicted W impurity density $\langle n_W\rangle$ and total W emissivity $\langle\epsilon_{tot}\rangle$, along with the measured $\langle\epsilon_{tot,m}\rangle$ profiles from bolometry are shown in figure 24 for the same two pulses #104681 and #105508. These are more peaked than the equivalent profiles across the LFS

[20] The relative isotope mass is defined as $A_{eff}=\sum(c_iA_i)/\sum c_i$, where $A_i\equiv m_i/m_p$ is the mass number and $c_i=n_i/n_e$ the concentration of each hydrogenic isotope (H, D and (*T*).

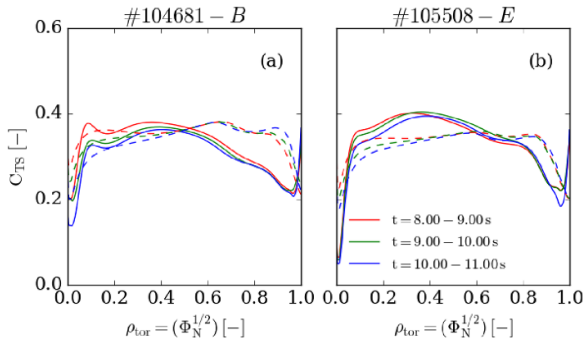

Figure 21. Profiles of the temperature screening parameter C_{TS} vs' normalised radius ρ_{tor}, calculated using FACIT for the two, matched 2.1 MA/3.85 T hybrid-scenario pulses #104681 in DT (left) and #105508 in D (right) with the input profiles shown in figure 20 for the three time ranges indicated in the figure, showing cases both with rotation ($M_{\phi,i} \neq 0$, solid) and without rotation ($M_{\phi,i} = 0$, dashed).

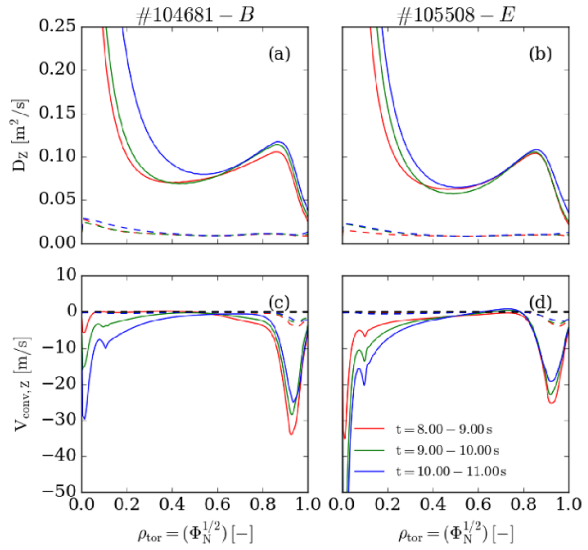

Figure 22. Profiles of the NC W diffusion coefficient $D_{NC,Z}$ and convection velocity $V_{NC,Z}$ vs' normalised radius ρ_{tor} calculated using NEO for the input profiles shown in figure 20 for the two, matched 2.1 MA/3.85 T hybrid-scenario pulses #104681 in DT (left) and #105508 in D (right).

mid-plane shown in figure 23 because the concentration of the heavy W impurities to the LFS by the strong toroidal rotation evident in the latter profiles is averaged out in the FSA profiles.

In the DT pulse #104681, the measured $\langle \epsilon_{tot,m} \rangle$ profiles are quite well reproduced by the modelling, except for some emission at mid-radius which might be due to the mid-Z Ti impurities ($A_{Ti} = 47.9, Z_{Ti} = 22$), detected by VUV spectroscopy, which are absent from the modelling.

As discussed above in section 3.6 in relation to the two D pulses #102813 and #102825, the hollowness of the measured FSA $\langle \epsilon_{tot,m} \rangle$ profiles over the pedestal gradient region is probably due to 'spill-over' of emission from outside the separatrix, especially from the lower HFS region, that is absent from the calculations. This is likely to be a result of the finite resolution of the bolometer system and of the tomography algorithm.

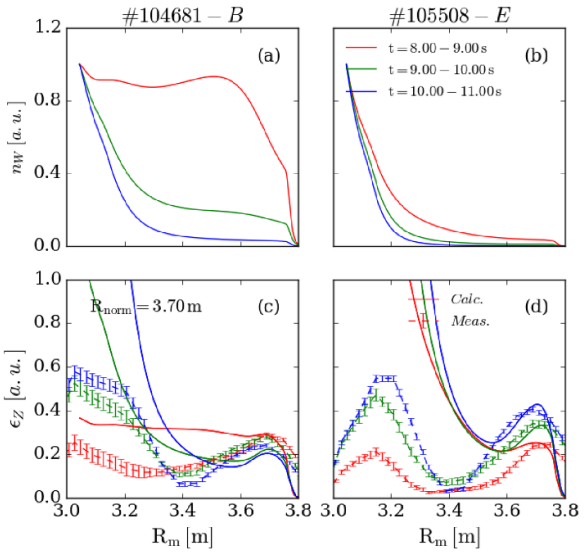

Figure 23. Profiles across the LFS mid-plane vs' major radius R_m, of: (*a*), (*b*) the W density n_W (normalised to 1 at the magnetic axis); and (*c*), (*d*) the measured total emissivity from bolometer tomography ϵ_{tot} (dashed) and the calculated total emissivity of W $\epsilon_{tot,W}$ (solid), where the latter is normalised to the former at $R_m = 3.7$ m, for the two, matched 2.1 MA/3.85 T hybrid-scenario pulses #104681 in DT (left) and #105508 in D (right), calculated using the transport coefficients from FACIT shown in figure 22.

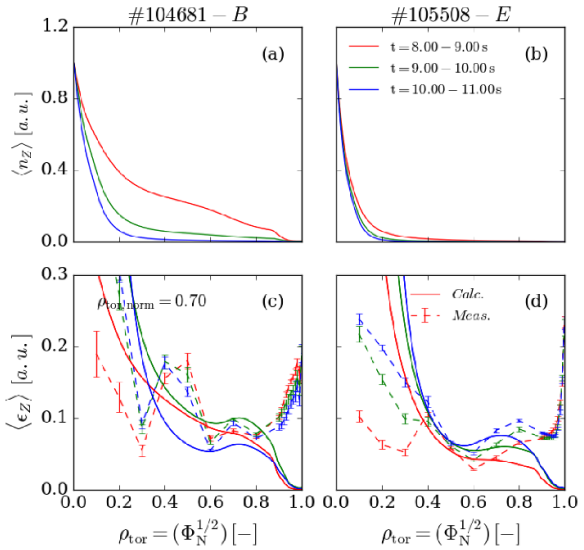

Figure 24. Flux-surface-averaged (FSA) profiles vs' ρ_{tor} of: (*a*), (*b*) the W density $\langle n_W \rangle$ (normalised to 1 at $\rho_{tor} = 0$); and (*c*), (*d*) the total emissivity $\langle \epsilon_{tot} \rangle$ from bolometer tomography and the calculated total emissivity of W $\langle \epsilon_{tot,W} \rangle$ (where the latter is normalised to the former at $\rho_{tor} = 0.7$), for the two, matched 2.1 MA/3.85 T hybrid-scenario pulses #104681 in DT (left) and #105508 in D (right), calculated using the transport coefficients from FACIT shown in figure 22.

In the D pulse #105508, the predicted W $\langle \epsilon_{tot} \rangle$ profiles are too peaked compared to the more modest degree of peaking observed in the bolometric measurements, i.e. too great

a degree of W accumulation is predicted by the FACIT modelling. Possible explanations for this have already been discussed in section 3.6 above.

4.6. Discussion of the D to DT comparison

Here, the main results of our analysis and modelling comparing the matched pair of 2.1 MA/2.85 T hybrid-scenario pulses #104681 in DT and #105508 in D are summarised.

Similarly low radiated power fractions implies that impurity contamination remains well controlled in both of these pulses, which are remarkably similar in several other respects: with the same stored energy $W_{\rm pl}$ at the same heating power, the energy confinement is also similar; both the line-average $\bar{n}_{\rm e}$ and pedestal $n_{\rm e,ped}$ densities are similar, hence, so is the density peaking; the pedestal parameters $T_{\rm i,ped}$ and $\Omega_{\phi\,{\rm i,ped}}$ are also remarkably similar; as is the ELM frequency at $f_{\rm ELM} \sim 40-60\,{\rm Hz}$.

Both pulses exhibit only a modest degree of core impurity accumulation, this gradually increasing in the D pulse #105508 due to increasing density peaking. Analysis of the vertical bolometer camera data reveals that on average the DT pulse exhibits modest inter-ELM W screening ($(\Delta\bar{n}_{\rm W}/\bar{n}_{\rm W})_{\rm i-ELM} \sim -0.3 \pm 0.3\%$ per ELM cycle), while in the D pulse the screening behaviour is considerably stronger ($\sim -2.9 \pm 0.4\%$).

As input to the NC W transport modelling with FACIT, the Mach number $M_{\phi,{\rm i}} \sim 0.35$ and collisionality $g \sim 2\times10^{-3}$ over the mantle region are similar in both pulses, while $M_{\phi,{\rm i}}$ is significantly higher in the core of the D pulse ($\sim$0.4) than in the DT pulse ($\sim$0.35). The effect of rotation is to decrease the screening parameter $C_{\rm TS}$ over the mantle region more in the DT than in the D pulse, while it increases $C_{\rm TS}$ more in the core of the D pulse.

For DT pulse, $R/L_{T_{\rm i}} \sim 2R/L_{n_{\rm i}}$ over most of profile, while for D pulse $R/L_{T_{\rm i}} > 2R/L_{n_{\rm i}}$ over the mantle region just inside pedestal top. As a result, the W convection is *slightly* positive over this region in the D pulse, while the W convection is generally inwards in the DT pulse, except early in the pulse, when there is NC screening in the core.

In both of the pulses, the FACIT modelling predicts too strong W accumulation in the core compared to the measurements from the bolometer tomography[21]. This disagreement is more evident in the emissivity profiles at the LFS midplane than in the FSA profiles, which is an indication that there is likely to be a significant contribution to the measured total emissivity $\epsilon_{\rm tot}$ from lower mass, mid-Z impurities, e.g. Ti and Ni.

Possible reasons for the discrepancy between the observations of inter-ELM W screening from analysis of the bolometer data and the NC modelling with FACIT are discussed in section 5 below.

[21] Note that this is also the case if $T_{\rm i}$ data from the main-ion CXRS system is used instead of that from the Ne impurity CXRS.

5. Discussion

Possible causes for the discrepancy between our observations of inter-ELM W screening from bolometry and results of our modelling of the NC W transport for these pulses must relate to deficiencies in either: the observations the inter-ELM W flushing/screening from analysis of the bolometry data and/or in the NC W transport modelling using FACIT.

Considering first the W screening observations:

The measurement technique for determination of the W ELM flushing/screening from the bolometry data cannot be used to evaluate the W transport during the highly dynamic phase during and immediately following the ELM events. The low-pass filtering ($f_{\rm LP} < 200\,{\rm Hz}$) applied to the fast bolometry data results in 'ringing' of the signal during the $\sim$10 ms following the ELMs, which cause a spike in the measured intensity due to the influx of W into the SOL and subsequent strong emission as impurities reach a steady ionisation balance. For this reason, we set our post-ELM averaging window long enough after the ELM peak ($\sim\mathcal{O}(10\,{\rm ms})$) to omit this initial post-ELM period. Hence, our analysis is blind to what might occur during this initial post-ELM phase.

Time-dependent impurity transport during this initial post-ELM period might affect the results. For example, inward convection due to the sudden steepening of the $n_{\rm e}$ gradient over the mantle region following the ELMs might cause the W impurities to move inwards towards the core, where their total emissivity $\mathcal{R}_\epsilon$ is lower than in the mantle region, hence resulting in apparent 'screening' behaviour. However, because the radiated power $P^{\rm Pl}_{\rm Rad}$ remains steady and controlled during these pulses, any inward W transport must be balanced by an outward diffusive or convective flux later during the inter-ELM periods, otherwise the impurity content of the core plasma and hence the radiated power would continually increase.

Secondly, two possible discrepancies in our modelling of the NC W transport are: (a) inadequacies in measurement of the kinetic profiles over the pedestal gradient region input to FACIT; and (b, c) possible incompleteness of the modelling of the NC transport.

a) Potential inadequacies in the edge CXRS measurements of the ion temperature $T_{\rm i}$ and toroidal rotation $\Omega_{\phi,{\rm i}}$ over the pedestal gradient region have been discussed before in [5]. Further FACIT runs have been performed to quantify the effect of $T_{\rm i}$ and/or $\Omega_{\phi,{\rm i}}$ for the main D^+ (or T^+) possibly being lower over the pedestal gradient region than that measured by the CXRS systems on the Ne^{10+} impurity ions. Blending the edge $T_{\rm i}$ profile smoothly into the steeper $T_{\rm e}$ profile over this region is found not to be sufficient alone to result in positive NC W convection across the pedestal. However, also reducing $\Omega_{\phi,{\rm i}}$ to zero across this region as well as steepening the $T_{\rm i}$ gradient is sufficient to achieve W screening across the pedestal, resulting in a hollow FSA W density profile. However, there would have to be very strong departures from the measurements of both $T_{\rm i}$ and $\Omega_{\phi,{\rm i}}$ over the pedestal gradient region for this to be the case.

We might expect that CX collisions between the D^+ ions and background neutrals might cause them to rotate less rapidly than the Ne^{10+} impurity ions on which the CXRS measurements were made. However, on DIII-D, which has a main-ion CXRS system [53], the main ion D^+ rotation has been measured to be higher than that of the C^{6+} impurities, running contrary to this hypothesis.

The influence on our modelling results of applying different weights to the T_i data from the core and edge CXRS systems, which often differ in the peripheral region where the measurement points overlap, has also been investigated using additional FACIT runs. Giving more weight to the T_i data from the core system, which often measures somewhat higher values than the edge system, does not result in positive NC convection in the region just inside the pedestal top, where W screening was observed in the earlier pulse #97781 of [5]. Hence, this is unlikely to be the cause of the lack of W screening across the pedestal gradient region found in our modelling results.

b) Calculations of the NC impurity transport using the drift-kinetic code NEO for a case from the JET-Be/W pulse #99602 (a low density ITB scenario pulse with input power $P_{in} \sim 26\,MW$) with both W as a trace impurity and an experimentally relevant concentration of Ni ($\sim 0.1\%$, contributing a $\Delta Z_{eff} \sim 1$), have revealed significant differences in the predicted transport coefficients from those obtained using FACIT for W as a single trace impurity [54].

In particular, the W convection velocity from the NEO calculations, which include the W flux driven by collisions between the W and the Ni impurities, was found to be positive ($V_{NC,Z} \sim 15\,m\,s^{-1}$) across the outer core plasma ($0.5 \lesssim \rho_{tor} \lesssim 0.8$) rather than negative ($\sim -5\,m\,s^{-1}$) as predicted using FACIT.

Similar, recent calculations using NEO for the hybrid scenario pulse #102813, discussed above in section 3, assuming a constant Ni concentration contributing a $\Delta Z_{eff} = 1$, also show the W convection velocity to be weakly positive ($V_{NC,Z} \sim 1\,m\,s^{-1}$), rather than close to zero across the core plasma as predicted using FACIT with both W and Ni impurities, where the Ni is included by running FACIT twice for W with a D background plasma and then with Ni as the background plasma at the relevant density [55].

Note that a similar change in $V_{NC,Z}$ could be produced by increasing R/L_{T_i} by a factor $\times 1.1$ and decreasing R/L_{n_i} by $\times 0.9$ from the measured values, which indicates the rather high sensitivity of the sign of the calculated W convection to measurement uncertainties.

These differences between the NEO and FACIT calculations are thought to be due to the poloidal weighting of the fluxes driven by collisions between the Ni and W being important for the relatively heavy Ni impurity in a rotating plasma. This effect is not considered in FACIT, which treats the concentration of other (typically low-Z) impurities as constant on flux surfaces.

c) Under the relatively high-collisionality ($10^{-3} \lesssim g \lesssim 10^{-2}$) conditions of the pedestal gradient region compared to the core plasma, the high mean charge state of the W impurities ($\bar{Z} \sim \mathcal{O}(20)$) in these hot pedestals with $T_{e,ped} \gtrsim 1\,keV$, means that the parameter $g^\star$ relevant to the non-local transport effects mentioned above in section 3.5.1 can exceed unity. In this case, parallel friction between the main ions and impurities can result in an appreciable poloidal (up-down) asymmetry of the impurity density and a reduction of the radial particle flux.

The 'Maget' branch of FACIT, which can model this situation has been run for one of the pulses #102813 discussed here, the results showing that this is indeed the case, with an $\mathcal{O}(1)$ up-down asymmetry developing in the W density. Such effects may explain the up-down asymmetry of the peripheral total emissivity, seen particularly clearly in the DT pulse #104681 in figure 16.

6. Conclusions

Analysis of data from the vertical viewing bolometer camera using our technique for determining the change in W content of the plasma due to ELMs and inter-ELM cross-pedestal transport reveals significant 'screening' behaviour, i.e. negative changes in $(\Delta \bar{n}_W/\bar{n}_W)_{i-ELM}$ during the inter-ELM periods, during the four pulses discussed here, which were optimised during the scenario development described in [12] to maximise the W screening.

This optimisation was achieved by reducing the fuelling during the initial heating ramp to produce a hot, low collisionality pedestal, with strong toroidal rotation, both of which favour peripheral impurity screening [5]. Reducing the plasma current from 2.3 MA to 2.1 MA reduced $n_{e,ped}$ by $\sim 25\%$, resulting in a concomitant increase in $T_{i,ped}$ and further enhancement of the screening behaviour.

A successful transfer of the scenario to to DT operation was achieved by increasing B_t from 3.45 T to 3.85 T, thereby compensating the decrease in L/H-threshold power P_{LH} in DT compared to D, which otherwise induced an earlier L/H transition. A matched pulse in D was later run using earlier gas fuelling at a lower rate, resulting in the pair of pulses in DT and D with remarkably similar confinement and pedestal properties, which are analysed in detail here.

In both of these pulses, radiation levels remained low and controlled throughout the pulse, with only modest impurity accumulation, with the bolometry analysis revealing significantly stronger inter-ELM W screening behaviour in the D than the DT pulse.

Predictive modelling of the NC W impurity transport using the FACIT code [9] of the four pulses analysed in detail here has failed to explain the apparent peripheral W screening behaviour. The predicted W convection is always strongly inward across the pedestal gradient region ($V_{NC,Z} \sim \mathcal{O}(50\,m\,s^{-1})$). Also, the predicted W convection across the plasma radius is typically weak ($V_{NC,Z} \sim 0$) at mid-radius, with outward convection predicted across the core only at the earliest times considered in two of the four pulses discussed here. Only in the D pulse #105508 is the NC convection slightly positive ($V_{NC,Z} \lesssim \mathcal{O}(1\,m\,s^{-1})$) just inside the pedestal top, but far

less so than that observed ($V_{\mathrm{NC},Z} \lesssim \mathcal{O}(25\,\mathrm{m\,s^{-1}})$) in the earlier pulse #97781 from [5].

The total emissivity ϵ_{tot} profiles, calculated using the predicted NC transport coefficients for W as the sole impurity, show better agreement with the measured FSA profiles $\langle\epsilon_{\mathrm{tot}}\rangle$ from bolometer tomography than with $\epsilon_{tot}(R)$ measured across the LFS mid-plane, which indicates there may be missing emission from mid-Z impurities, that are not included in the modelling.

Possible explanations for the discrepancy between the W screening observations based on bolometry analysis and the NC W transport modelling, discussed in section 5, relate either to deficiencies in the analysis technique or in our NC W transport modelling.

It may be that a significant fraction of the cross-pedestal W transport occurs during the immediate post-ELM phase, which the analysis technique is unable to resolve.

Using the NEO code, it has also been shown that collisions between the mid-Z impurity Ni at experimentally relevant concentrations ($\sim\mathcal{O}(0.1\%)$) and W, modelled as a trace impurity, can result in more positive W convection across the core plasma than as predicted using FACIT, even reversing the direction from inward to outward. Further such NEO calculations for the pulses discussed here could be performed, once reliable estimates of the relevant Ni concentration profiles become available from integrated analysis.

It might also be that non-local effects, relevant at the higher collisionality of the pedestal gradient region (where the parameter $g^{\star} > 1$), result in an appreciable up-down poloidal asymmetry of the high-Z W impurity density, which might reduce the cross-pedestal W flux. Such effects would be worthy of further detailed study and could also be important in explaining recent results from ASDEX-U experiments to reproduce peripheral W screening in hybrid-scenario plasmas [56]. In these experiments, significant differences between profiles of the total emissivity measured at the top of the plasma and at LFS mid-plane have been observed in high-resolution A-XUV bolometry measurements.

Another possibility is that W screening takes place outside of the separatrix, perhaps with poloidal $E\times B$ drifts localising the W impurities to a 'stagnation' region at the lower HFS region, as discussed in [57, 58]. However, if this were the case, it would be difficult to reconcile this with the observations of inter-ELM screening from our bolometry analysis.

Acknowledgment

This work has been carried out within the framework of the EUROfusion Consortium, funded by the European Union via the Euratom Research and Training Programme (Grant Agreement No. 101052200 - EUROfusion) and from RCUK Energy Programme (Grant No. EP/W006839/1). Views and opinions expressed are however those of the author(s) only and do not necessarily reflect those of the European Union or the European Commission. Neither the European Union nor the European Commission can be held responsible for them. ITER is the Nuclear Facility INB No. 174. The views and opinions expressed herein do not necessarily reflect those of the ITER Organization. To obtain further information on the data and models underlying this paper please contact PublicationsManager@ukaea.uk.

ORCID iDs

A.R. Field 0000-0003-0671-9668
C. Angioni 0000-0003-0270-9630
I.S. Carvalho 0000-0002-2458-8377
P. Carvalho 0000-0002-8480-0499
A. Chomiczewska 0000-0003-4931-728X
D. Fajardo 0000-0001-5802-4572
L. Frasinetti 0000-0002-9546-4494
J.M. Fontdecaba 0000-0001-7678-0240
J. Hobirk 0000-0001-6605-0068
A. Kappatou 0000-0003-3341-1909
D. Keeling 0000-0002-3581-7788
D. Kos 0000-0002-9550-4329
B. Labit 0000-0002-0751-8182
E. Lerche 0000-0003-4584-3581
H. Sun 0000-0003-0880-0013
N. Vianello 0000-0003-4401-5346
S. Wiesen 0000-0002-3696-5475

References

[1] Hirshman S.P. and Sigmar D.J. 1981 *Nucl. Fusion* **21** 1079
[2] Angioni C. *et al* 2021 *Plasma Phys. Control. Fusion* **63** 073001
[3] Dux R., Loarte A., Fable E. and Kukushkin A. 2014 *Plasma Phys. Control. Fusion* **56** 124003
[4] Dux R., Loarte A., Angioni C., Coster D., Fable E. and Kallenbach A. 2017 *Nucl. Mater. Energy* **12** 28–35
[5] Field A.R. *et al* 2023 *Nucl. Fusion* **63** 016028
[6] Matthews G.F. *et al* 2011 *Phys. Scr.* **T145** 014001
[7] Bigot B. *et al* 2019 *Nucl. Fusion* **59** 112001
[8] Hobirk J. 2023 *Nucl. Fusion* **63** 112001
[9] Fajardo D., Angioni C., Casson F.J., Field A.R., Maget P. and Manas P. 2023 *Plasma Phys. Control. Fusion* **65** 035021
[10] Garcia J. *et al* 2022 *Phys. Plasmas* **29** 032505
[11] Kappatou A. *et al* 2024 *Plasma Phys. Control. Fusion* **67** 045039
[12] King D. *et al* 2025 Development of hybrid plasmas in D and DT for impurity screening *30th IAEA Fusion Energy Conf.* (*Tianfu International Conference Centre, Chengdu, China, 13–18 October 2025*) EX-C (available at: https://conferences.iaea.org/event/392/papers/35907/files/13833-IAEA%20proceedings%20D%20King%20JET%20hybrids.pdf)
[13] Lao L., St. John H., Stambaugh R.D., Kellman A.G. and Pfeiffer W. 1985 *Nucl. Fusion* **25** 1611
[14] Appel L.C. and Lupelli I. 2018 *Comput. Phys. Commun.* **223** 1–17
[15] Andrew Y. and Hawkes N.C. 2006 *Rev. Sci. Instrum.* **77** 10E913
[16] Bartiromo R., Bombarda F., Giannella R., Mantovani S., Panaccione L. and Pizzicaroli G. 1989 *Rev. Sci. Instrum.* **60** 237
[17] Loarte A. *et al* 2004 *Phys. Plasmas* **11** 2668–78
[18] Fussmann G., Field A.R., Kallenbach A., Krieger K. and Steuer K.H. (The ASDEX Team) 1991 *Plasma Phys. Control. Fusion* **33** 1677

[19] Lerche E. *et al* 2016 *Nucl. Fusion* **56** 036022
[20] Casson F.J. *et al* 2015 *Plasma Phys. Control. Fusion* **57** 014031
[21] Hender T.C. *et al* 2016 *Nucl. Fusion* **56** 066022
[22] Ingesson L.C. *et al* 1998 *Nucl. Fusion* **38** 1675
[23] Huber A. *et al* 2007 *Fusion Eng. and Design* **82** 1327–34
[24] Field A.R. *et al* 2021 *Plasma Phys. Control. Fusion* **63** 095013
[25] Fedorczak N. *et al* 2015 *J. Nucl. Mater.* **463** 85–90
[26] Sertoli M. *et al* 2018 *Rev. Sci. Instrum.* **89** 113501
[27] Henderson S.S., Bluteau M., Foster A., Giunta A., O'Mullane M.G., Pütterich T. and Summers H.P. 2017 *Plasma Phys. Control. Fusion* **59** 055010
[28] Hinton F.L. and Wong S.Z. 1985 *Phys. Fluids* **28** 3082–98
[29] Angioni C. and Hender P. 2014 *Plasma Phys. Control. Fusion* **56** 124001
[30] Fajardo D., Angioni C., Maget P. and Manas P. 2022 *Plasma Phys. Control. Fusion* **64** 055017
[31] Belli E.A. and Candy J. 2008 *Plasma Phys. Control. Fusion* **50** 095010
[32] Belli E.A. and Candy J. 2009 *Plasma Phys. Control. Fusion* **51** 075018
[33] Belli E.A. and Candy J. 2012 *Plasma Phys. Control. Fusion* **54** 015015
[34] Helander P. and Sigmar D.J. 2002 *Collisional Transport in Magnetised Plasmas* 1st edn (Cambridge University Press)
[35] Helander P. 1998 *Phys. Plasmas* **5** 3999
[36] Fülöp T. and Helander P. 1999 *Phys. Plasmas* **6** 3066–75
[37] Fülöp T. and Helander P. 2001 *Phys. Plasmas* **8** 3305–13
[38] Maget P., Frank J., Nicolas T., Agullo O., Garbet X. and Lütjens H. 2020 *Plasma Phys. Control. Fusion* **62** 025001
[39] Maget P., Manas P., Frank J., Nicolas T., Agullo O. and Garbet X. 2020 *Plasma Phys. Control. Fusion* **62** 105001
[40] Romanelli M. *et al* 2014 *Plasma Fusion Res.* **9** 3403023
[41] Pasqualotto R. *et al* 2004 *Rev. Sci. Instrum.* **75** 3891–3
[42] Negus C.R., Giroud C., Meigs A.G., Zastrow K.-D. and Hillis D.L. 2006 *Rev. Sci. Instrum.* **77** 10F102
[43] Dickinson D., Saarelma S., Scannell R., Kirk A., Roach C.M. and Wilson H.R. 2011 *Plasma Phys. Control. Fusion* **53** 115010
[44] Summers H.P. *et al* 2001 The ADAS manual version 2.3 (available at: http://adas.ac.uk)
[45] Angioni C., Mantica P., Pütterich T., Valisa M., Baruzzo M., Belli E.A., Belo P., Casson F.J., Challis C., Drewelow P., Giroud C., 2014 *Nucl. Fusion* **54** 083028
[46] Erba M., Cherubini A., Parail V.V., Springmann E. and Taroni A. 1997 *Plasma Phys. Control. Fusion* **39** 261
[47] Bizarro J.P.S. *et al* 2016 *Plasma Phys. Control. Fusion* **58** 105010
[48] Potzel S. *et al* 2015 *J. Nucl. Mater.* **463** 541–5
[49] Huber A. *et al* 2020 *Nucl. Mater. Energy* **25** 100859
[50] Chomiczewska A. *et al* 2024 *Nucl. Fusion* **64** 076058
[51] Reinke M.L. *et al* 2012 *Plasma Phys. Control. Fusion* **54** 045004
[52] Wesson J.A. *et al* 1997 *Nucl. Fusion* **37** 578
[53] Haskey S.R. *et al* 2018 *Plasma Phys. Control. Fusion* **60** 105001
[54] Maggi C.F. *et al* 2025 Core and edge transport of scenario with internal transport barrier in tritium and deuterium-tritium plasmas in JET with Be/W wall *30th IAEA Fusion Energy Conf. (FEC-2025)* (*Tianfu International Conference Centre, Chengdu, China*, *13–18 October 2025*) EX-C (available at: https://conferences.iaea.org/event/392/papers/35834/files/13863-Maggi_FEC2025_EX11_1_preprint.pdf)
[55] Fajardo F. 2025 private communication
[56] Kappatou A. *et al* 2025 Investigations of tungsten temperature screening in the periphery of ASDEX Upgrade plasmas *29th EU-US Transport Task Force Workshop* (*HUN-REN Centre for Energy Research, Budapest, Hungary*, *9–12 September 2025*) (available at: https://ttf2025.ek.hun-ren.hu/abstracts/)
[57] Korving S.Q. *et al* 2022 Modelling of high-field-side high-density region with the nonlinear MHD code JOREK with kinetic neutrals *48th EPS Conf. on Plasma Physics* (*Virtual*, *27 June–1 July 2022*) vol O3 p 105 (available at: https://indico.fusenet.eu/event/28/contributions/251/attachments/265/850/EPS_paper_2022_SQ_Korving.pdf)
[58] Rozhansky V. *et al* 2021 *Nucl. Fusion* **61** 126073